Available online at www.sciencedirect.com
SCIENCE DIRECT®
Journal of Nuclear Materials 323 (2003) 313–340
journal of nuclear materials
www.elsevier.com/locate/jnucmat

Cleavage fracture and irradiation embrittlement of fusion reactor alloys: mechanisms, multiscale models, toughness measurements and implications to structural integrity assessment

G.R. Odette [a,*], T. Yamamoto [a], H.J. Rathbun [a], M.Y. He [a], M.L. Hribernik [a], J.W. Rensman [b]

[a] *Department of Mechanical and Environmental Engineering, University of California Santa Barbara, 3343 Engineering II, Santa Barbara, CA 93106, USA*
[b] *NRG P.O. Box 25, 1755 ZG Petten, The Netherlands*

Abstract

We describe the highly efficient master curves–shifts (MC–ΔT) method to measure and apply cleavage fracture toughness, $K_{Jc}(T)$, data and show that it is applicable to 9Cr martensitic steels. A reference temperature, T_0, indexes the invariant MC shape on an absolute temperature scale. Then, T_0 shifts (ΔT) are used to account for various effects of size and geometry, loading rate and irradiation embrittlement (ΔT_i). The paper outlines a multiscale model, relating atomic to structural scale fracture processes, that underpins the MC–ΔT method. At the atomic scale, we propose that the intrinsic microarrest toughness, $K_\mu(T)$, of the body-centered cubic ferrite lattice dictates an invariant shape of the macroscopic $K_{Jc}(T)$ curve. $K_{Jc}(T)$ can be modeled in terms of the true stress–strain (σ–ε) constitutive law, $\sigma\ (T,\epsilon)$, combined with a temperature-dependent critical local stress, $\sigma^*(T)$ and stressed volume, V^*. The local fracture properties, $\sigma^*(T)$–V^*, are governed by coarse-scale brittle trigger particles and $K_\mu(T)$. Irradiation (and high strain rate) induced increases in the yield stress, $\Delta\sigma_y$, lead to ΔT_i, with typical $\Delta T_i/\Delta\sigma_y \approx 0.6 \pm 0.15$ °C/MPa. However, ΔT_i associated with decreases in σ^* and V^* can result from a number of potential non-hardening embrittlement (NHE) mechanisms, including a large amount of He on grain boundaries. Estimates based on available data suggest that this occurs at >500–700 appm bulk He. Hardening and NHE are synergistic, and can lead to very large ΔT_i. NHE is signaled by large (>1 °C/MPa), or even negative, values of $\Delta T_i/\Delta\sigma_y$ (for $\Delta\sigma_y < 0$), and is often coupled with increasing amounts of intergranular fracture. The measured and effective fracture toughness pertinent to structures almost always depends on the size and geometry of the cracked body, and is typically significantly greater than K_{Jc}. Size and geometry effects arise from both weakest link statistics, related to the volume under high stress near a crack tip, and constraint loss associated with large amounts of deformation in small specimens and shallow surface cracks. We describe micromechanical models that can be used to adjust the toughness measured using small specimens to both the intrinsic material K_{Jc} and the effective toughness pertinent to a structure. Finally, using a simple example, we illustrate the profound implications of size-geometry effects on the fracture of fusion structures. This assessment is based on a metric of strength and ductility, specified as the ratios of the critical load and displacement at fracture to the corresponding yield load and displacement, P_c/P_y and Δ_c/Δ_y, respectively. Even in cases where the material experiences very brittle elastic fracture in standard tests, or in heavy sections, with $P_c/P_y < 1$, the extrinsic factors pertinent to fusion structures (small

* Corresponding author. Tel.: +1-805 893 3525; fax: +1-805 893 8651.
E-mail address: odette@engineering.ucsb.edu (G.R. Odette).

doi:10.1016/j.jnucmat.2003.08.023

shallow cracks in thin sections, etc.) lead to $P_c/P_y > 1$ and $\Delta_c/\Delta_y \gg 1$. Indeed, in some circumstances, the benefits of irradiation due to increases in P_c may more than offset the liabilities of the decreases in Δ_c.

PACS: 62.20.Mk; 61.82.−d

Nomenclature

Symbols

A	stressed area
A^*	critical stressed area
A_0	non-dimensional stressed area
A_{ssy}	stressed area under small SSY
$A_{P\Delta}$	area under elastic–plastic P–Δ curve
a	crack length
B	specimen thickness
B_r	reference thickness
b	ligament size
C^*_{He}	critical bulk He for IG fracture
CF	nominal constraint factor ($=\sigma_n/\sigma_y$)
C_K	proportional coefficient when $\Delta T_i \approx C_K(T_0)\Delta\sigma_y$
$C_0, C_1, C_2, \ldots$	polynomial fit parameters for $A_0 = f(\sigma_n/\sigma_y)$
d_{tp}	effective trigger particle size
D	non-dimensional deformation parameter
D^*	radiation enhanced diffusion coefficient
E'	plain strain elastic modulus
$f(a/W)$	non-dimensional function for K_I
f_{He}	critical fraction of monolayer coverage by He on a grain boundary for IG fracture
h_1, h_3	geometric factor for EPRI J estimation scheme
J	J-integral
J_c	critical J
J_e	elastic $J(=K_I^2/E')$
J_{ec}	critical elastic J $(=K_{Ic}^2/E')$
J_p	plastic J
K_{ax}	cleavage crack arrest toughness in single crystal
K_{cl}	K_J under conditions of constraint loss giving the same A as for SSY
K_g	Griffith cleavage toughness
K_I	Mode I stress intensity factor
K_{Ic}	linear elastic fracture toughness
K_{Ix}	cleavage initiation toughness in single crystal
K_{Ie}	effective fracture toughness
K_J	K derived from J by $K_J = \sqrt{JE'}$
K_{Jc}	critical K_J for fracture
K_{Je}	effective K_{Je}
K_{Jm}	measured K_{Jc}
K_{Jr}	reference K_{Jc} at $B_r = 25.4$ mm
K_{JB}	K_{Jc} adjusted to thickness B_r
K_{min}	cleavage threshold K_{Jc}
K_0	median K_{Jc} or K_{Jr} (at $P_f = 0.63$)
K_{0r}	a median reference value of K_0
K_μ	microcrack arrest fracture toughness
k_t	microcrack tip stress intensity factor
m_k	Weibull toughness modulus
m_σ	Weibull stress modulus
N	strain hardening exponent
p	B-scaling exponent
P_f	fracture probability
P	load
P_y	load at general yield
P_c	critical load at fracture
P_{ce}	P_c in elastic fracture regime
P_{co}	P_c in unirradiated condition
r	radial distance from crack tip
r_b	He bubble radius
$T_{c'}$	cleavage temperature from a simple model
T_0	master curve reference temperature
T_{0a}	adjusted reference temperature
T_{0i}	T_0 in irradiated condition
T_{0u}	T_0 in unirradiated condition
V^*	critical stressed volume for cleavage
V_σ	volume under high stresses near a crack tip
W	specimen width
W^*	critical specimen width leading to cleavage
x	distance from the crack tip at $\theta = 0$
Z_{LL}	non-dimensional loadline compliance
α	power law $\sigma(\varepsilon)$ fit parameter
δ	crack tip opening displacement
Δ	load point displacement
Δ_c	load point displacement at fracture
Δ_{co}	Δ_c in unirradiated condition
Δ_y	load point displacement at general yield
ΔN	change in N due to irradiation
ΔT_0	reference temperature shift
ΔT_{ci}	Charpy impact test ΔT
$\Delta T_{k'}$	ΔT_0 due to loading rate
ΔT_i	ΔT_0 due to irradiation
ΔT_g	ΔT_0 due to specimen size and geometry
ΔT_m	ΔT_0 for safety margin
$\Delta\sigma_y$	yield stress increase due to irradiation

ε	plastic strain
ε'	strain rate
ε_y	yield strain
γ	surface energy for fully brittle fracture
γ_p	plastic work/area for semi-brittle fracture
λ^*	critical distance
θ	angle from the crack plane
σ	stress
$\sigma(\varepsilon, \varepsilon', T)$	true stress–strain constitutive law
σ_{at}	athermal contribution of σ_y
σ_{ta}	thermally activated contribution of σ_y
σ_n	stress normal to the crack plane
σ_y	yield stress
σ^*	critical cleavage stress
σ_w	Weibull stress
σ_u	Weibull stress at $P_f = 0.63$
σ_{min}	minimum Weibull stress

Acronyms

BDT	brittle–ductile transition
CL	constraint loss
CT	compact tension specimen
FE	finite element
FW&B	first wall and blanket structure
IG	intergranular fracture
ITER	International Thermonuclear Fusion Experimental Reactor
IEA	International Energy Agency
MC	master curve
MC–ΔT	master curves–shifts method
NDE	non-destructive examination
NHE	non-hardening embrittlement
NFA	nanocomposited ferritic alloy
PAG	prior austenite grain
RKR	Ritchie, Knott and Rice
RO	Ramberg–Osgood
RPV	reactor pressure vessel
3PB	three point edge cracked bend specimen
SSY	small scale yielding
LSY	large scale yielding

1. Introduction

Since cracks will be presumed to be present, defect tolerant structural integrity assessments will be required to design and safely operate fusion reactor first wall and blanket (FW&B) structures. Integrity assessments must properly relate pertinent characteristics of both the *material and structure* to the *loads and displacements* (or stresses and strains) that lead to fracture by sudden crack extension. The pertinent characteristics include the specific size and geometry of cracked-body and appropriate measures of the material's constitutive properties and fracture toughness. While generally not an issue at the start-of-life, the probability of fast fracture increases in service due to the growth of sub-critical cracks by fatigue and other mechanisms, as well as the degradation of fracture toughness by irradiation embrittlement.

To begin, it is important to define 'fracture toughness' since it has both different values and significance in its various manifestations [1]. [1] Further, the *effective* toughness of a cracked body *extrinsically* depends on size and geometry. Indeed, fracture toughness can be considered an *intrinsic material property* only for very restricted and well-defined conditions. These conditions are seldom met in practice. In this paper, we define a material fracture toughness (K_{Jc}) for plane strain, elastic–plastic small scale yielding (SSY) conditions under quasi-static Mode I loading for through-thickness edge fatigue cracks with a depth (a) to width (W) ratio of $a/W \approx 0.5$. However, even in this very restricted case, K_{Jc} itself depends on the specimen thickness, or the crack front length (B). Thus, we will further define a reference $K_{Jc}(K_{Jr})$ for a specified reference $B_r = 25.4$ mm. These defined values will generally differ significantly from the measured fracture toughness (K_{Jm}), and typically even more so for the effective toughness (K_{Je}) pertinent to the fracture of a cracked structure.

Tempered 9Cr martensitic steels, such as F82H and Eurofer97, are the prime candidate alloys for International Thermonuclear Fusion Experimental Reactor (ITER) blanket test modules and demonstration fusion power reactor FW&B structures [2,3]. They typically contain 7–9%Cr and a few percent Mo or W (≈1–2% nominally, or about 2 times the Mo wt% equivalent) in the low activation variants, <0.1%C and smaller amounts of other alloying elements like V and Ta. Typical heat treatments include normalizing in the range of 1000 ± 50 °C, followed by tempering in the range of 750 ± 30 °C for 0.5–3 h, resulting in yield stress (σ_y) levels of $\approx 525 \pm 50$ MPa. The corresponding cleavage fracture transition temperature regime is below −50 °C and the ductile tearing toughness is more than 200 MPa $\sqrt{m}$. Alloy microstructures are characterized by tempered lath/lath packet structures in prior austenitic grains (PAG) and a variety of fine (M_2C) and courser scale ($M_{23}C_6$) carbides; the largest carbides are on PAG

[1] For example, quasi-static versus dynamic, initiation versus arrest, fast cleavage versus ductile tearing and different combinations of loading modes I to III. Ref. [1] provides an excellent and comprehensive coverage of many of the basic fracture mechanics concepts used in this paper and is recommended as a source of background information on this topic.

boundaries. The sub-grain dislocation structures are complex but can be crudely represented by a density of $\approx 3 \pm 2 \times 10^{14}/m^2$. Many of the issues discussed in this paper also apply to so-called nanocomposited ferritic alloys (NFA) [3]. The NFAs typically have $\approx 13 \pm 2\%$Cr and $\approx 2 \pm 1\%$W and are strengthened to $\sigma_y \approx 1000 \pm 200$ MPa by an ultrahigh density of nm scale clusters of Y, O, and Ti at total solute contents of $\approx 1\%$. NFAs are processed by mechanical alloying and hot consolidation of powders resulting in small grain sizes ($\leqslant 5$ μm). NFAs are at earlier stages of development, but offer the potential for higher temperature applications. A major challenge they face is achieving sufficient toughness without compromising high creep strength [3].

These Fe-based systems, along with other body-centered cubic (bcc) alloys, including refractory vanadium, tungsten and molybdenum, all share several key characteristics that must be properly understood and managed.

- Between lower and upper shelf regions, K_{Jc} increases with increasing test or service temperature (Fig. 1(a) and (b)). Fast fracture occurs due to unstable propagation of a macroscopic pre-existing crack by locally brittle cleavage or quasi-cleavage in most of this so-called transition region. We note that locally brittle fracture can also occur by intergranular (IG) processes; and that cleavage may follow a limited amount of ductile tearing. However, these fracture modes will not be the major focus of this paper.
- There is a large inherent scatter in K_{Jc} (or K_{Jr}), thus toughness is more properly described by a distribution function defined by the mean ($\langle K_{Jc} \rangle$), median (termed K_0, which in E1921 is for the reference K_{Jr}) and statistical confidence intervals (Fig. 1(a)).
- A variety of in-service microstructural evolutions, driven by the combination of elevated temperature and irradiation, often lead to significant hardening ($\Delta\sigma_y$) and the degradation of K_{Jc}. Embrittlement is manifested as an increase in a reference temperature (T_0), or ΔT_i, at a reference median value (K_0) of K_{Jc}, as well as reduction in the upper shelf tearing toughness (Fig. 1(b)).
- The effective and measured fracture toughness (K_{Je} and K_{Jm}) depend on size, geometry and loading rate of the cracked body, as well as other extrinsic factors that must be accounted for in practice.
- Most fracture tests on irradiated alloys will continue to be based on small to ultrasmall specimens.

We have previously described a systematic and highly efficient approach to dealing with embrittlement, as well as all the other factors that control the K_{Jm} and K_{Je}, known as the master curves–shifts (MC–ΔT) method

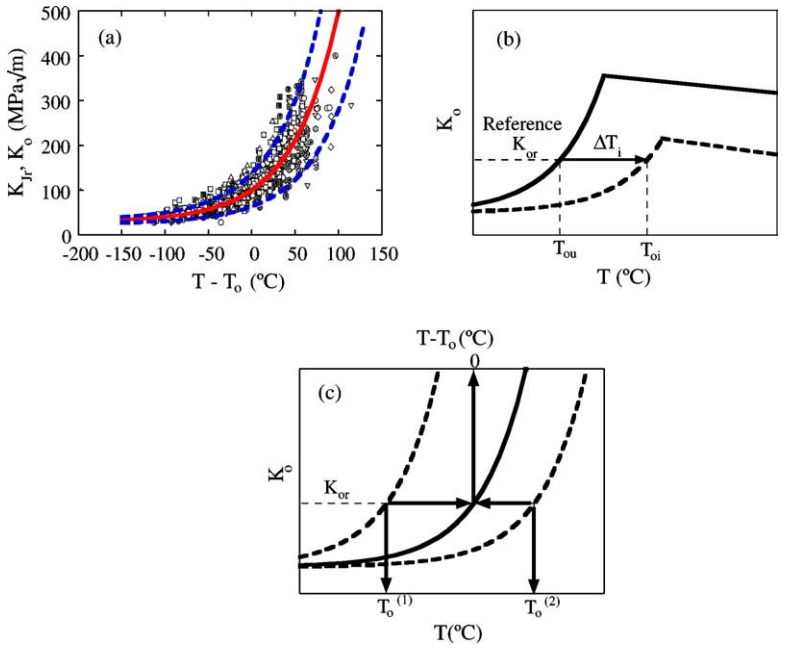

Fig. 1. (a) Illustration of unirradiated (open symbols) and irradiated (filled symbols) K_{Jr} data for RPV steels and the corresponding median $K_0(T)$ and 5 and 95% $K_{Jr}(T)$ master curves (MC) (courtesy M. Sokolov), (b) illustration of the effect of irradiation on $K_0(T)$ curves and ductile tearing toughness, (c) illustration of the MC method for positioning $K_0(T)$ curves (dashed lines) on an invariant $K_0(T - T_0)$ scale (solid line).

[4–8]. While differing in detail and philosophy, the MC–ΔT method extends from the American Society for Testing and Materials (ASTM) E1921 Master Curve Standard to evaluate median $K_0(T)$ and corresponding curves at specified confidence intervals ($K_{Jr}(T)$ at the 5% and 95% bounds) in the transition [9,10]. Both ASTM E 1921 and the MC–ΔT method *assume* there is a universal invariant toughness temperature curve shape, $K_0(T - T_0)$, or small family of shapes, that is indexed on an absolute temperature (T) scale by a reference temperature (T_0) at a median reference toughness, K_0, typically 100 MPa $\sqrt{m}$ (Fig. 1(c)). The $K_0(T - T_0)$ found in E 1921 is primarily for low alloy pressure vessel steels, but this shape also appears to be applicable to cleavage fracture in martensitic steels and, perhaps, vanadium alloys [4,11]. [2]

However, the E 1921 Standard is primarily intended for application to thick-walled pressure vessels and piping and other heavy section structures. It is specifically for a T_0 referenced at a $K_0 = 100$ MPa $\sqrt{m}$ and $B_r = 25.4$ mm. For fusion applications, alternate reference conditions are preferable. The MC–ΔT method also allows for a small family of MC $K_0(T - T_0)$ shapes for various conditions, like dynamic versus static loading rates [4]. The reference T_0 for the alloy in the unirradiated condition is 'measured' and then adjusted (T_{0a}) by a set of temperature shifts (ΔT). The ΔT can account for the effects such as loading rate (k'), irradiation (i), various size and geometric factors (g) and a safety margin (m) as

$$T_{0a} = T_0 + \Delta T_{k'} + \Delta T_i + \Delta T_g + \Delta T_m. \quad (1)$$

As discussed below, all these ΔT can be measured and modeled independently. [3] Large ΔT_i may control the lifetime and operating limits of FW&B structures. However, the ΔT_g for small surface cracks in thin-walled structures has a large negative value that may mitigate the effects of ΔT_i.

Thus, ensuring that the integrity of FW&B structures against fast fracture will require unified and concurrent efforts to develop:

- High toughness, irradiation resistant steels with low T_0 and ΔT_i.
- Semi-empirical, physically based models to predict the various ΔT. For example, ΔT_i is a function of the combination of key material (e.g., starting composition and microstructure) and irradiation (e.g. temperature, flux, fluence and spectrum) variables. Reliable predictions of ΔT_i will require a close integration of models, experiments and a comprehensive database. The database will largely depend on innovative small specimen test methods.
- Integrated procedures to apply the K_{Jm}, measured in small specimen tests, to predict the behavior for actual large-scale FW&B structures as controlled by K_{Je}.

Fortunately, extensive research on reactor pressure vessel (RPV) steels has shown that hierarchical approaches can be used to model both the fundamental mechanics/micromechanics of fracture and irradiation embrittlement [12,13]. Among the more important features of these models is that they are microstructurally based, thus provide a detailed physical framework for integrating an enormous range of information. Pertinent information is derived from theory and sub-models, as well as closely integrated experiments.

The paper proceeds as follows. First, we briefly outline the processes that occur on various length scales that mediate cleavage and hierarchical models that can be linked to predict $K_{Jr}(T)$ and K_{Je} from K_{Jm}, as well as the various ΔT, including ΔT_i. We also address the fundamental physics and mechanics underlying the assumption of an invariant shape for the MC. We next review recent progress on the MC–ΔT method, with special emphasis on size scaling and the relationship between ΔT_i and irradiation induced increases in the yield stress ($\Delta\sigma_y$). We also briefly discuss possible non-hardening embrittlement (NHE) mechanisms, including high concentrations of He. Finally, we illustrate the practical implications of size scales and crack geometry in mediating the effective strength and ductility of thin-walled fusion structures.

A more detailed discussion of irradiation hardening and various forms of irradiation embrittlement is given elsewhere [14]. This reference summarizes the database on $\Delta\sigma_y$ and sub-sized Charpy impact test measurement of shifts (ΔT_c) for 9Cr martensitic steels in terms of the data trends represented by using simple fitting models. Significant limitations in the existing database are discussed. This reference also reviews information on the effect of He on hardening and embrittlement and the potential for NHE mechanisms at high He levels. This is followed by an assessment of future research needs, emphasizing the importance of understanding and modeling the combined effects of irradiation and metallurgical variables, including dose rate. 'Understanding' and developing robust models will require a well-designed database as well as both single variable and mechanism experiments. Characterizing the total alloy microstructure as well as the mechanical properties themselves will be critical.

[2] The E 1921 MC is $K_0 = 30 + 70\exp[0.019(T - T_0)]$ MPa $\sqrt{m}$. There are indications that the $K_0(T)$ curve for IG fracture cannot be represented by the MC shape for cleavage.

[3] For example ΔT_i can often be related to the increase in yields stress ($\Delta\sigma_y$), which in turn can be related to the changes in the microstructure of the material.

2. An overview of cleavage fracture and embrittlement mechanisms and models

In this section, we overview the processes occurring on various length scales, from atomic to structural, that mediate cleavage fracture. We also summarize a series of corresponding hierarchical *physical* sub-models that can be linked to *quantitatively* model cleavage fracture in components as well as coupon-scale test specimens. Ultimately, the multiscale models will be directly related to the microstructure, both for optimizing alloy properties and predicting the effects of irradiation and other service conditions. The models also treat the effects of size, geometry and loading rate. A simple flow chart summarizing these interrelations is shown in Fig. 2. We revisit this with an expanded flow chart in the summary Section 5.

2.1. The cracked- body at length scales 10^{-3} to >1 m (Fig. 3)

The term cracked-body refers to both actual structures and coupon-type test specimens. Pertinent structural and coupon length scales range from about 10^{-3} to >1 m (Fig. 3(a) and (b)). The size and geometry of the cracked region potentially subject to plastic deformation plays a key role in determining the critical loads and displacements (P_c–Δ_c) resulting in the rapid propagation of a cleavage crack (Fig. 3(c) and (d)). The crack itself and surrounding elastic–plastic region, are generally much smaller ($\ll$1 m) than the structure itself. Thus, fast fracture conditions can usually be defined in terms of the P_c–Δ_c on properly defined elastic boundaries surrounding the cracked location. Other sources of local stress due to temperature gradients and residual strains, as well as the effects of loading modes and structural compliance, must also be treated in evaluating P_c–Δ_c. For simplicity, we will consider load controlled fracture of a through edge-cracked beam in three point bending (3PB), characterized by width (W), thickness (B), crack length (a), uncracked ligament length ($b = W - a$) and span (S) (Fig. 3(b)).

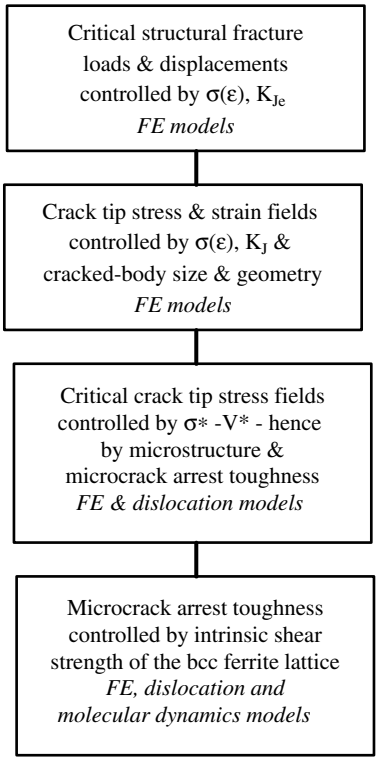

Fig. 2. Simplified flow chart of hierarchical multiscale modeling approach to linking atomic to structural scale processes that mediate cleavage fracture.

The pertinent crack loading parameter that relates the load (P) and load point displacement (Δ) to the concentrated stress and strain fields that develop at the tip of a crack (see below) that cause cleavage depends on length scales and non-dimensional geometric factors. For very large, deeply cracked bodies, where loading is linear elastic and plasticity is confined to a small, embedded region near the crack tip, the pertinent parameter is the stress intensity factor, K_I [1]. The K_I is determined by P, the crack length (a) and a known non-dimensional geometric factor, $f(a/W)$, as

$$K_I = f(a/W)(P/BW)\sqrt{a}. \tag{2}$$

The elastic region is limited to the initial linear portion of the P–Δ curve (Fig. 3(d)) up to the point of plastic yielding (P_y–Δ_y). Elastic fracture occurs at $P = P_{ce} < P_y$ (Fig. 3(d)) when $K_I = K_{Ic}$, where K_{Ic} is the material's linear elastic fracture toughness. Other specimen configurations and complex cracked-bodies can also be treated in terms of non-dimensional geometric factors and a crack length parameter such as a. As discussed below, K_{Ic} also depends on the crack front length, B.

Since P_{ce}/P_y for a given K_{Ic} increases with $1/\sqrt{a}$, at a sufficiently small size (a), the cracked body undergoes general yielding at P_y–Δ_y (Fig. 3(d)). This results in a non-linear permanent *plastic* displacements with $\Delta > \Delta_y$. The curve in Fig. 3(d) is a typical elastic plastic P/P_y versus Δ/Δ_y curve for an edge cracked beam with $a/W = 0.5$ in 3-point bending (3PB). For $P > P_y$ the plastic zone around the crack tip is no longer well confined within a much larger elastic region. In this case, the most appropriate crack loading parameter is the elastic–plastic J-integral [1],

$$J = J_e + J_p. \tag{3a}$$

The elastic J_e and K_I are related as $K_I = \sqrt{J_e E'}$ where E' is the plane strain elastic modulus. The plastic J_p is a

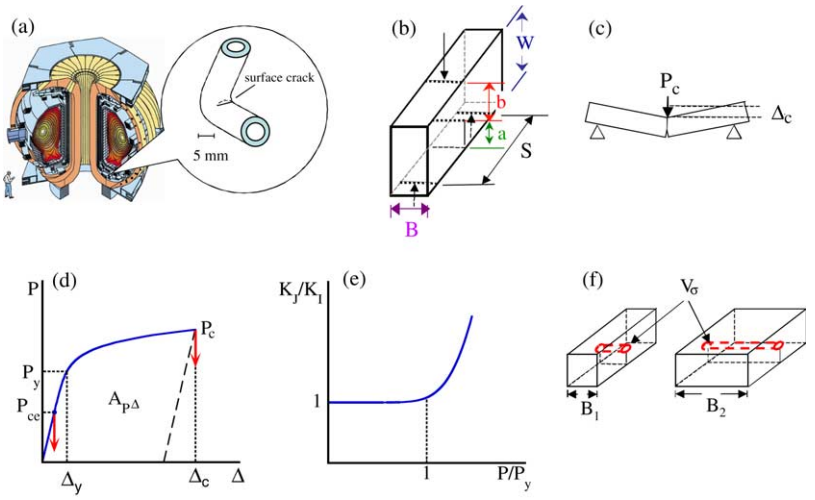

Fig. 3. (a) Illustration of a typical shallow surface crack in a thin-walled tube that is part of a large fusion FW&B structure, (b) a typical 3PB specimen with key dimensions, (c) illustration of the critical P_c and Δ_c at fast fracture, (d) illustration of a P–Δ curve with both fracture and general yielding P and Δ and the $A_{P\Delta}$ used to evaluate J_p, (e) K_J/K_I as a function of P/P_y, (f) illustration of a larger V_σ for a longer crack front length B.

function of geometric factors and the area under the elastic–plastic ($\Delta > \Delta_y$) P–Δ curve, $A_{P\Delta}$ (Fig. 3(d)). For a beam in 3PB [1],

$$J_p \approx 2A_{P\Delta}/bB. \tag{3b}$$

Note, it is common to represent J in terms of an equivalent $K_J = \sqrt{JE'}$. We will use K_J and K_{Jc} in the remainder of this paper. Fig. 3(e) shows the corresponding K_J/K_I as a function of P/P_y.

For only somewhat less restricted conditions as compared to the linear elastic case (still deep cracks in bending with a deformation parameter $D = K_J^2/(E'b\sigma_y) < 0.01$ – see below), fracture occurs when $K_J = K_{Jc}$ [1]. In general, if these conditions are violated, K_{Jm} (or K_{Je}) is greater than K_{Jc}, due to so-called loss of constraint (see below). In the elastic–plastic regime K_J and P–Δ also depend on the *constitutive properties* $[\sigma(\varepsilon, \varepsilon', T)]$ of the material, characterized by a true-stress (σ), true-plastic strain (ε) law that is a function of ε, temperature (T) and strain rate (ε'). The $\sigma(\varepsilon)$ can be actual data for a particular material, or a simple analytical representation such as a Ramberg–Osgood (RO) formulation [1] to describe *plastic* strain ($\varepsilon > \varepsilon_y$) hardening, as

$$\varepsilon = \alpha[\sigma/\sigma_y]^{1/N-1}[\sigma/E]. \tag{4}$$

Here $\alpha \approx 1$ is a fit parameter, and N (<1) is the (fitted) strain hardening exponent. The K_J and corresponding P–Δ for a specified cracked body size and geometry and $\sigma(\varepsilon)$ can be computed based on finite element (FE) methods using codes such as ABAQUS [15].

An additional extrinsic geometric factor in cleavage fracture is the statistical effect of the *volume* (V_σ) of material under high stresses near a crack tip (Fig. 3(f)). Larger V_σ lead to a higher probability of sufficiently stressing the weakest link(s) of a large population of potential trigger sites for nucleating propagating microcracks that lead to macroscopic cleavage fracture. The fracture probability is typically described by Weibull statistics [16–22]. For a given K_J, V_σ increases with the length of the crack front, or B for through-cracked, plane strain specimens. As discussed in Sections 3 and 4, this leads to an approximate scaling of K_{Jc} with $B^{-1/4}$.

As a consequence of statistical and constraint loss (CL) effects, small, shallow surface cracks in compliant thin-wall structures primarily under tensile loading manifest a much higher K_{Je} compared to either deep through cracks in bending in standard test specimens; or even larger cracks in thick-walled pipes and pressure vessels. The combination of a $K_J > K_I$ and a higher K_{Je} in a thin section structure also leads to a larger effective ductility ($\Delta_c \gg \Delta_y$), providing benefits much akin to post-yield tensile ductility. We return to the factors leading to large and beneficial Δ_c/Δ_y in Section 4.

Irradiation influences fracture processes at the macroscopic cracked-body level through its effect on $\sigma(\varepsilon)$ and K_{Jc}. Advanced, physically-based fracture mechanics methods are needed to combine the extrinsic factors and properties to predict P_c–Δ_c limits for wide range of structural conditions. Likewise, the fracture toughness database will be largely based on small specimen testing, raising essentially all of the same issues.

2.2. Crack blunting and process zone stress (and strain) fields at length scales from 10^{-6} to 10^{-3} m (Figs. 4 and 5)

In structural alloys, loading a cracked body to K_J results in blunting of the crack tip to an opening δ (Fig. 4(a)) and the development of a plastic zone over a region scaling with $(K_J/\sigma_y)^2$ [1]. Closer to the crack tip, at distances defined by $r(\theta)$, or x in the $\theta = 0$ crack plane, the local stresses are greatly elevated. The key stress normal to the crack plane (σ_n) reaches peak levels up to $\sigma_n \approx 3$–$5\sigma_y$ (Fig. 4(a) and (b)) depending on N [1]. For example, if $\sigma_y = 650$ MPa, the peak $\sigma_n \approx 2500$ MPa for $N = 0.1$. At sufficiently high σ_n the local mode of fracture is most often cleavage (or quasi-cleavage), involving the rapid propagation of brittle trigger particle nucleated microcracks, with very little local plastic deformation and associated energy dissipation. This leads to a flat-faceted fracture surface (see Fig. 4(c) for various fracture surface morphologies).

The high σ_n acts over distances that scale with δ or $K_J^2/(E'\sigma_y)$ in a region known as the process zone, where cleavage fracture initiates [1]. The high σ_n is due to the combination of strain hardening and tri-axial stress-state *constraint* imposed by the non-uniformly de-

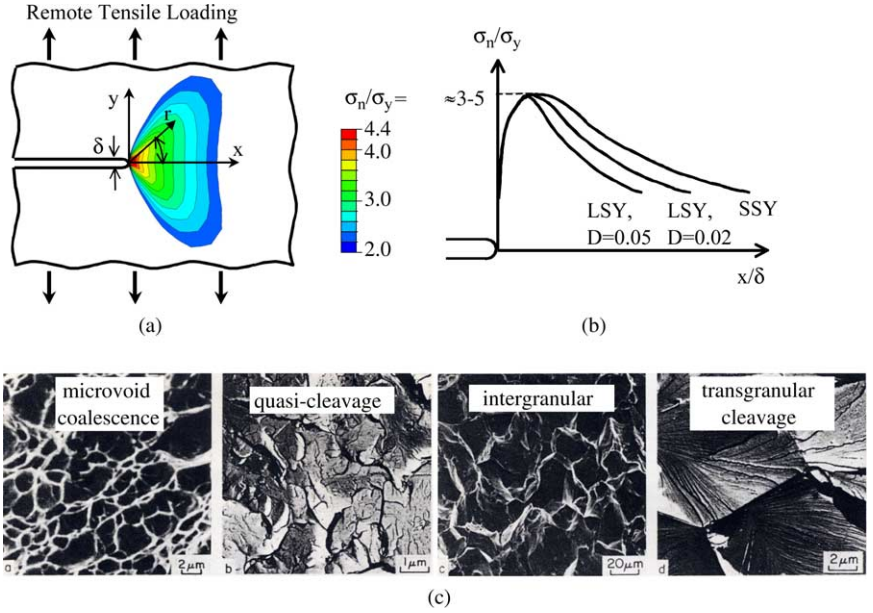

Fig. 4. (a) Illustration of a blunting crack tip stress field and increasing $\sigma_n > \sigma_y$ contours with decreasing r, (b) illustration of crack plane σ_n fields for SSY and large scale yielding (LSY), (c) micrographs showing various types of local fracture modes.

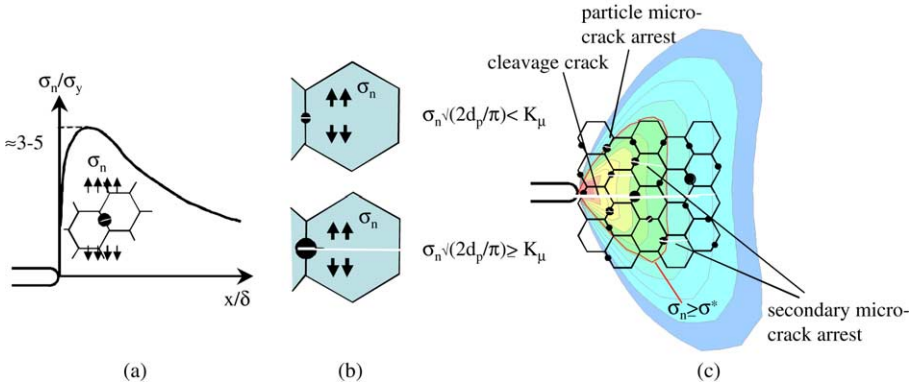

Fig. 5. (a) Illustration of carbide cracking near the peak σ_n stress region of a blunting crack, (b) illustration of conditions for microcrack propagation into the ferrite matrix, versus arrest at the trigger particle interface, (c) illustration of a large number of stressed and some cracked particles with only a few successfully propagating microcracks.

formed material surrounding the crack tip region. For certain well-defined conditions, [4] known as SSY, the fields are self-similar in non-dimensional distance, $r/\delta \approx r/\ [K_J^2/(2E'\sigma_y)]$, and are uniquely determined by K_J, E' *and* $\sigma(\varepsilon)$ [1]. As discussed below, the high σ_n fields must reach a critical level ($\sigma_n = \sigma^*$) that encompasses a sufficient volume of trigger particle microstructure in front of the crack tip to cause cleavage [1,4–7,16–32].

More generally, however, the crack tip σ_n fields are also sensitive to extrinsic factors related to the size, geometry and loading configuration of the cracked body and the level of plastic deformation [1]. We will define a non-dimensional parameter $D = 2\delta/b = K_J^2/(E'\sigma_y b)$, that is the ratio of the length scale of the high σ_n fields to the uncracked ligament length, b. In almost all-practical situations, the amplitude of the fields at a given K_J is *reduced* from the SSY limit, due to the *loss of constraint*, which increases with increasing D (Fig. 4(b)) [1,4,6,23–30]. [5] *CL* increases the K_{Jm} and K_{Je} at cleavage. Indeed, in the limit of severe CL, the local fracture mode may change from cleavage to ductile tearing. CL also occurs for shallow cracks and for tensile versus bending dominated loading conditions, due to compressive stress fields (a so-called T-stress) in the direction of crack propagation [1,4,21,26–30]. Note that statistical (depending on B) and CL effects (depending on geometry, D and B) interact to increase K_{Je} [22–25]. That is, small cracks stress smaller local volumes, hence, require a higher K_{Jc} for cleavage that, in turn, results in more CL that leads to even higher K_{Je}.

The effect of irradiation on the crack tip fields is *primarily* due to corresponding changes in $\sigma(\varepsilon, \varepsilon', T)$, as reflected in $\Delta\sigma_y$ and ΔN. At a specified N, the amplitude of the σ_n increases in direct proportion to σ_y. In this case, $\Delta T_i \approx C_K(T_0)\Delta\sigma_y$, where C_K ($\approx$0.6 °C/MPa) (see below and [5,31]). However, depending on the temperature dependence of the local fracture stress (see below), C_K may, or may not, depend on both the T_0 of the unirradiated steel and $\Delta\sigma_y$ [5,31]. The σ_n decreases with reductions in strain hardening ($\Delta N < 0$) due to irradiation. To some extent, this counteracts the effect of $\Delta\sigma_y$ on the crack tip fields, resulting in smaller ΔT_i. Irradiation induced reductions in N also amplify CL. These complex effects are reasonably understood, and can be modeled assuming the deformation remains relatively homogeneous. However, irradiation can also result in localization of flow. The effects of the localization of deformation in slip bands or, in the limit, narrow channels, are not well understood. In general, however, localization appears to play a secondary role in cleavage fracture. In part, this may be due to the fact that flow localization tends to be suppressed at high strains and under multi-axial stress states.

2.3. Micromechanics of cleavage and the role of microstructure at length scales of 10^{-7}–10^{-5} m (Figs. 5 and 6)

In order to proceed further in understanding and modeling cleavage, it is necessary to invoke a micromechanical model. The underpinning model was first proposed by Ritchie, Knott and Rice (RKR) [32]. The RKR model is based on the observation that cleavage occurs by the propagation of microcracks emanating from brittle trigger-particles, like large grain boundary carbides, that are subject to the high process zone stress fields (σ_n) near a blunting crack (Fig. 5(a)). Local stress–strain concentrations due to incompatible matrix-particle deformation cause some of the brittle ceramic trigger-particles to crack. However, most often the critical event is the *propagation* of the dynamic microcrack from the broken particle into the tougher ferrite matrix (Fig. 5(b)). In many cases, particle nucleated microcracks arrest. However, a microcrack continues to propagate if the local normal stress ($\sigma_n \gg \sigma_y$) reaches a critical value ($\sigma_n = \sigma^*$) that depends on the size and orientation of the cracked trigger particle (d_{tp}) and, as discussed below, the microarrest toughness of the ferrite matrix (K_μ). Note, small clusters of carbides are a favorable site for the nucleation of a propagating microcrack, since they have an effective d_{tp} that is larger than those of the individual particles themselves [4,29,30]. Assuming a cleavage orientated penny-shaped particle crack

$$\sigma^* \approx K_\mu(\pi/2d_{tp})^{1/2}. \tag{5}$$

Experimental estimates of K_μ based on measurements of d_{tp} and σ^* range from about 1.5 to 4.0 MPa $\sqrt{m}$ (for example, see data compilations in [33–35]). A $\sigma^* \approx 2000$ MPa for the average of 2.75 MPa $\sqrt{m}$ and $d_{tp} = 3$ μm is reasonably consistent with the $K_{Jc}(T)$ for 9Cr martensitic steels. The K_μ can be expressed in terms of a modified Griffith fracture criteria [1]

$$K_\mu = [2E'(\gamma + \gamma_p)]^{1/2}. \tag{6}$$

Here, γ is the surface energy of the cleavage plane for fully brittle Griffith-type fracture and γ_p is the excess plastic work per unit area of fracture surface associated with discrete dislocation activity near the crack tip. For (1 0 0) fracture, taking $\gamma_{100} \approx 2$ J/m^2 and $E'_{100} \approx 150$ GPa gives the Griffith cleavage toughness $K_g \approx 0.77$ MPa $\sqrt{m}$, close to typical estimates of <1 MPa $\sqrt{m}$ [36,37]. Note, in some publications the standard elastic

[4] Standard SSY conditions are defined for $a/W \approx 0.5$ in loading geometries dominated by bending (versus tension).

[5] There is a large literature on this topic covering a variety of approaches to treating CL effects. The papers cited here are among those most relevant to the proposed MC–ΔT method.

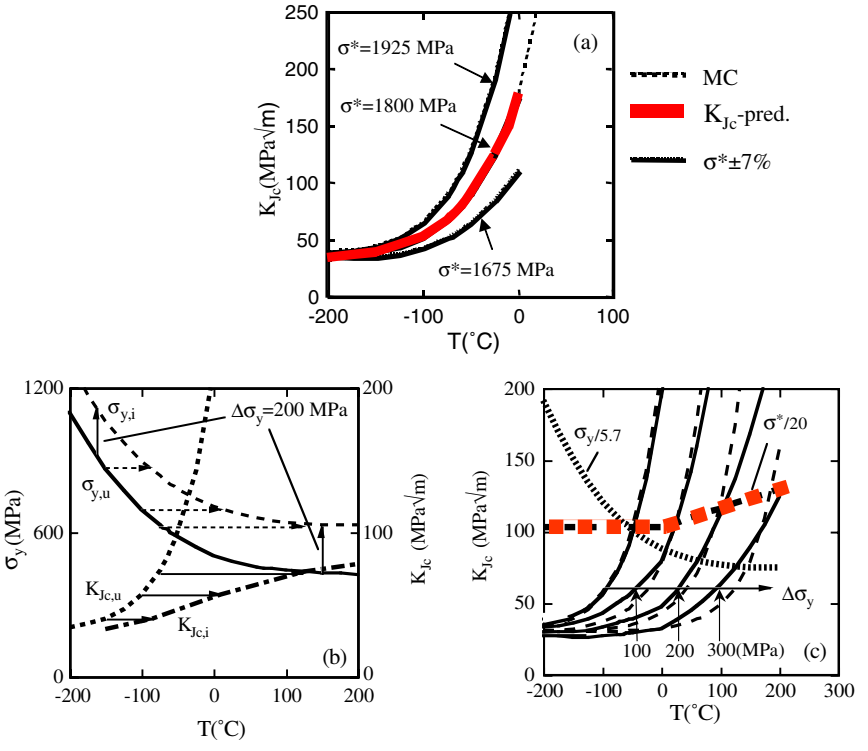

Fig. 6. (a) The $K_{Jc}(T)$ predicted by the σ^*–V^* model (heavy solid lines) compared to the MC (dotted line) for $T_0 = -45$ °C, (b) illustration of the predicted layover of the $K_{Jc}(T)$ curve for a $\Delta\sigma_y = 200$ MPa if σ^* is not a function of temperature, (c) the $K_{Jc}(T)$ predicted by the σ^*–V^* model (solid lines) compared to MCs for $\Delta\sigma_y = 100$, 200 and 300 MPa (dashed lines) assuming $\sigma^*(T)$ is a function of temperature as shown by the fitted heavy dashed line.

plane strain Young's modulus, with $E' \approx 225$ GPa, is incorrectly used giving a nominal $K_\mu \approx 1.35$ MPa $\sqrt{m}$. Assuming a typical maximum trigger particle size of $d_{tp} \approx 3$ μm, σ^* is ≈560 MPa. Both K_g and σ^* are much lower than typical experimental estimates.

Larger effective K_μ and γ_p are associated with crack arrest at internal boundaries (such as lath packet and at grain boundaries) [34] and for the coalescence of multiple arrested microcracks in the case of quasi-cleavage [4,22,29,30] (see below and Fig. 4(c)). Typically, the microcrack facets form at different heights relative to the average position of the crack plane. The facets link by shear of the transverse ligaments and macroscopic cleavage occurs when the microcracks ultimately coalesce, forming a larger unstable process zone crack [26]. Quasi-cleavage is typical for martensitic steels with many internal lath and packet boundaries [4,26,29,30]. In this case, both stress (cleavage facet nucleation) and strain (shear linking and coalescence of microcracks) mediated processes lead to the final instability of a larger process zone crack [4,29,30]. However, we believe that the initial propagation of the microcracks from the trigger particles is still the necessary event that *controls* fracture for most microstructures and test conditions, [6] since the final instability occurs over a very small

[6] Most tests are carried out under load control, or with load train compliances that do not detect microcrack damage, with a detectable pop-in-type load drop, before unstable propagation of the process zone crack. While microcrack propagation following secondary arrest (see Figure 5c) does require a higher γ_p, this is still typically a small fraction of the elastic plastic J needed to set up the critical stress fields in the first place. The γ_p is much smaller for the primary particle propagation event (with smaller cracks), but it still requires roughly the same amount of macroscopic J. Further, the cracks arrested at interfaces are larger (d_g), thus the critical local stress intensity factor scales with the higher $\sqrt{\gamma_p/d_g}$, and not $\sqrt{\gamma_p}$. This is further evident in the similarity of $K_{Jc}(T)$ (master?) curves for alloys which do not experience secondary arrest events. That is by the time the primary microcracks form, it does not 'cost' much more J to link them to form an unstable process zone crack. The more general point is that it is not the energy of the local fracture event itself that directly controls K_{Jc}, but rather the energy to create the local conditions that it takes to make it happen in the first place.

increment of loading after the microcracking initiates [4,29,30]. Thus, if the microcrack arrest toughness is an intrinsic characteristic of the bcc ferrite lattice, and is not sensitive to the alloy microstructure, then the invariant $K_0(T - T_0)$, in principle, can be related to the intrinsic temperature dependence of $K_\mu(T)$ and $\sigma_y(T)$.

The $\sigma_n = \sigma^*$ at cleavage condition requires the combination of the high constraint at a blunting crack tip ($\sigma_n \gg \sigma_y$) and sufficiently large σ_y (or more properly the local $\sigma(\varepsilon)$). For unirradiated alloys, σ_y is large enough only at low temperature. However, irradiation elevates σ_y and $\sigma(\varepsilon)$, resulting in shifts in the cleavage transition to higher temperatures (ΔT_i). In some cases, irradiation, or other service conditions, may also decrease σ^*, leading to NHE. RKR also noted that that a sufficiently high $\sigma_n = \sigma^*$ alone was in sufficient to define K_{Jc} at cleavage. They postulated that cleavage occurs when the critical stress acts over a critical distance, λ^*, related to the characteristic spacing between the large trigger particles; λ^* is typically a small multiple of the grain size, since larger carbides are located on grain boundaries. The classical RKR model assumes that both σ^* and λ^* are relatively independent of temperature, consistent with the corresponding insensitivity of E' and γ (but not necessarily γ_p). While it contains the key physics governing cleavage, the RKR model *does not predict* the observed $K_{Jc}(T)$ at higher toughness.

Both cleavage and quasi-cleavage involve the collective interactions of a number of crack-tip processes that *cannot be described* fully by the simple λ^* criterion. We (and others) have proposed an alternative model that cleavage, by either a single or few propagating microcracks, or quasi-cleavage involving extensive microcracking prior to cleavage, occurs when the $\sigma_n = \sigma^*$ encompass a critical *area* (A^*), or more generally *volume*, $V = V^* = B[A(\sigma_n = \sigma^*) = A^*]$, near the crack tip [4–8,23–30]. Here, $A(\sigma_n)$ is the in-plane area within a specified σ_n stress contour averaged over the crack front length, B.

While recognizing a similar microstructural role of trigger particles themselves, the σ^*–V^* local fracture criteria reflects the experimental observation that cleavage usually initiates in the region of peak σ_n, rather than at a fixed distance (i.e., λ^*) from the crack tip. This distance increases with lower $\sigma_y(T)$ and increasing $K_{Jc}(T)$ as the temperature increases [4,5,26,29,30,38]. Further, the $\sigma_n \geqslant \sigma^*$ region must act on a large population of potential trigger particles, estimated to be $\approx 10^5$ in total and ≈ 100 of the largest features (Fig. 5(c)). Indeed, many particles crack, but only the largest and most favorably oriented produce propagating microcracks. The σ^*–V^* model naturally links fatigue precrack fracture tests to blunt notch tests [39] under both static and impact loading; and, as shown below, this model is consistent with the MC $K_0(T)$ shape at low temperatures.

In principle, more elaborate weakest link-type statistical models better represent the physics of cleavage fracture ([16–24] and see below).

However, the σ^*–V^* local fracture criteria provides a simple, deterministic basis to model K_{Jc}, including the effects of irradiation and CL. Note that the V^* also serves as a reasonable surrogate for other stressed region criteria that may be more pertinent to the actual cleavage process, such as a wedge of material within $\pm\theta$ of the crack plane.

The in-plane stressed area $A(\sigma_n)$ in fracture tests increases with K_J. For SSY conditions $A_{ssy}(\sigma_n, K_J)$ increases with K_J^4, and cleavage occurs when at $A_{ssy}(\sigma^*, K_{Jc}) = A^*$. The A_{ssy} can be represented in a compact non-dimensional form (A_0) as [5,6,27]

$$A_0 = \log[A_{ssy}(\sigma_n/\sigma_y)\sigma_y^4/K_J^4]. \tag{7}$$

The $A_0(\sigma_n/\sigma_y)$ are computed using FE simulations for a specified $\sigma(\varepsilon)$, as represented by σ_y, E' and N. The numerical results for a given constitutive law can be fitted $(C_0, C_1, C_2, \ldots)$ to a polynomial as [5,6,27]

$$A_0(E'/\sigma_y, N, \sigma_n/\sigma_y) = C_0 + C_1(\sigma_n/\sigma_y) + C_2(\sigma_n/\sigma_y)^2. \tag{8}$$

Eqs. (6) and (7) can be used to evaluate K_{Jc} at specified values of $\sigma_n = \sigma^*$, $A_{ssy} = A^*$ and $\sigma_y(\varepsilon', T)$, as

$$K_{Jc}(T) \approx \sigma_y(T)\left[A \times 10^{A_0(n\cdot E', \sigma^*/\sigma_y)}\right]^{1/4}. \tag{9}$$

Thus, in the framework of this model, the microstructurally sensitive intrinsic material properties that control the SSY K_{Jc} are $\sigma(\varepsilon, \varepsilon', T)$, A^* and σ^*. The σ^* is controlled by the coarse-scale trigger particle microstructure *and* K_μ. Again, the K_μ may be an intrinsic property of the bcc ferrite lattice.

As noted previously, this and other RKR-type models also generally assumed that σ^* and V^* are insensitive to temperature and strain rate. This seems reasonable for V^*, since it depends directly on the coarse-scale trigger particle microstructure. Measurements based on blunt notch tests, where cleavage is controlled by a broadly peaked σ_n, also support the assumption that σ^* is approximately independent of temperature [31,33–35,40–44]. A corollary is that the inherent matrix K_μ is also temperature-independent. Fig. 6(a) shows the predicted SSY $K_{Jc}(T)$ for $\sigma^* = 1800 \pm 125$ MPa, for a nominal $\sigma_y(T)$, $A^* = 10^{-8}$ m^2, and $N = 0.1$ characteristic of unirradiated pressure vessel and martensitic steels. Note while the model is deterministic, it can also be cast in a statistical form by modeling expected specimen to specimen variations in σ^* and V^*. It is evident that for the low $T_0 \approx -45$ °C the shapes of the predicted curves are in good agreement with $K_0(T - T_0)$ shape shown as the dashed line.

However, we have previously shown that a temperature-independent σ^* and K_μ are *not* consistent with an invariant $K_0(T - T_0)$ for T_0 higher than ≈0 °C [5]. Large ΔT_0 shifts due to irradiation hardening ($\Delta\sigma_y$) can increase T_0 up to the range of 100 °C or more. Fine scale irradiation induced features, that have a major effect on $\Delta\sigma_y$ and $\sigma(\varepsilon, \varepsilon', T)$, are not expected to have a corresponding influence on σ^* and A^*. This assumes that the coarser scale trigger particle features do not change under irradiation and that K_μ is an intrinsic property of the ferrite matrix. However, a temperature independent σ^* and K_μ would result in a much lower slope in the predicted $K_{Jc}(T)$ curve for large $\Delta\sigma_y$, as illustrated in Fig. 6(b). The reduced slope of $K_{Jc}(T)$ is due to the temperature dependence of $\sigma_y(T)$ [5]. Specifically, ignoring modest effects of differences in strain hardening, the unirradiated and irradiated K_{Jc} *are the same* at equal unirradiated and irradiated σ_y, as shown by the horizontal arrows at various temperatures. Hence, the $\Delta T_i(T)$ increases with increasing temperature, since $d\sigma_y(T)/dT$ decreases. This reduces the slope of the irradiated $K_{Jc}(T)$ curve. This simple model predicts that there is an upper limit on K_{Jc} at sufficiently large $\Delta\sigma_y$ and that, in this case, that cleavage occurs at all test temperatures. Accounting for decreases in the strain hardening exponent N due to irradiation reduces the effects of hardening, but does not alter the basic trend towards a lower slope of the $K_{Jc}(T)$ curve with increasing $\Delta\sigma_y$ and ΔT_i. Such behavior has not been observed up to at least $\Delta\sigma_y \approx 200$ MPa where the $K_0(T - T_0)$ appears to be consistent with the MC shape for irradiated pressure vessel steels [45]. As discussed in Section 3.4, there is evidence of similar agreement for 9Cr martensitic steels up to even higher $\Delta\sigma_y > 350$ MPa [7].

As illustrated in Fig. 6(c), the predicted $K_{Jc}(T)$ *is* reasonably consistent with the $K_0(T - T_0)$ shape (dashed lines) at higher T_0, that would be associated with large irradiation induced $\Delta\sigma_y$ (here, 100, 200 and 300 MPa shown by heavy solid lines) assuming that there is a mild increase in $\sigma^*(T)$ with increasing temperature above ≈0 °C [5]. The model assumes that $\sigma^*(T)$ is not affected by irradiation, and that $\Delta\sigma_y$ is not a function of test temperature. The $K_{Jc}(T)$ curves for the various $\Delta\sigma_y$ account for modest reductions in strain hardening following irradiation. The $\sigma^*(T)$, shown by the heavy shaded-dotted line (scaled by a factor of 1/20), was estimated by fitting both the shapes of the $K_{Jc}(T)$ curves and ΔT_i as a function of $\Delta\sigma_y$. The predicted $\Delta T_i/\Delta\sigma_y \approx 0.68$ °C/MPa (see Fig. 13(b) below) is consistent with the pressure vessel steel data trend [45]. The unirradiated $\sigma_y(T)$ curve is also shown (scaled by a factor of 1/5.7). Note, depending on the precise $\sigma_y(T)$, N and ΔN used in the analysis, the modest temperature dependence of $\sigma^*(T)$ may begin somewhat below 0 °C, as was found in a similar analysis based on a statistical Weibull strength model [23].

However, the key result is that there is a specific and predictable relation between the effects of irradiation on $\sigma(\varepsilon, \varepsilon', T)$ *and* ΔT_i. We will discuss this further for 9Cr martensitic steels in Section 3.4. Note, the $\Delta T_{k'}$ for high loading rates can also be modeled in terms of the corresponding effect on $\sigma(\varepsilon, \varepsilon', T)$. The magnitude of $\sigma^*(T)$ is controlled by the size of the largest trigger particles ($d_{tp} \approx 3$ μm) and $K_\mu(T)$. Thus, within the framework of this model, the invariance of $K_0(T - T_0)$ for a range of microstructures, σ_y and T_0 is mediated by the underlying invariance of the intrinsic $K_\mu(T)$. Atomic lattice length-scale processes control $K_\mu(T)$.

2.4. Non-hardening embrittlement and the potential roles of He and H

Before discussing $K_\mu(T)$, it is important to note that embrittlement can also result from reductions in σ^* and/or V^* due to a number of mechanisms. In the case of such NHE, ΔT_i can even occur for conditions of softening when $\Delta\sigma_y$ is $\leqslant 0$. Combinations of $\Delta\sigma_y > 0$ and $\Delta\sigma^* < 0$ are synergistic, and lead to very large ΔT_i. Since this is such a broad topic, we will not attempt to provide specific references, but note that pertinent information can be found in a very large and diverse body of literature. Non-hardening contributions to irradiation embrittlement are signaled by large $\Delta T_i/\Delta\sigma_y > 1$, or even negative $\Delta T_i/\Delta\sigma_y$ for $\Delta\sigma_y < 0$. NHE has been observed for 9Cr martensitic steels for irradiation temperatures above ≈400 °C [14]. In many cases, NHE is accompanied by an increasing fraction of IG versus cleavage fracture [14]. In principle, IG NHE can be modeled in terms of an IG σ^*(IG) instead of the cleavage σ^*(CL). The σ^*(IG) is typically initially greater than σ^*(CL). In this case, transgranular cleavage is the preferred fracture path. However, if σ^*(IG) decreases in service more rapidly than σ^*(CL), cleavage will be gradually replaced by IG fracture which, under severe conditions, approaches 100%.

NHE occurs under thermal aging conditions even in the absence of irradiation. Mechanisms include: precipitation (e.g., Laves phase) or coarsening (e.g., carbides) of brittle trigger particles and instabilities of grain and sub-grain lath structures; segregation of impurity elements, like P, to grain boundaries (or desegregation of elements like C); and environmental interactions with H, as well as other processes that result in grain boundary weakening and damage such as creep cavity and methane bubble formation. Notably, significant NHE has been observed in 9Cr martensitic steels thermally aged up to 10,000 h at temperatures from 500 to 650 °C. The Charpy impact test transition temperature shifts after aging ranged from ≈20 °C (at 500 °C) to 90 °C (at 650 °C) [2,14,46,47]. Fortunately, $\Delta\sigma_y$ generally decreases with increasing temperature in regimes where many thermal processes may lead to significant decreases in σ^*.

However, irradiation would be expected to enhance thermal aging effects by a number of mechanisms [14]. For example, radiation enhanced diffusion would shift the C-curves for the precipitation of brittle phases to lower times and temperatures. Far too little attention has been paid to non-hardening irradiation embrittlement. Thus, detailed fractographic examinations, along with characterization of coarse scale microstructures, must be carried out in future embrittlement studies, including additional thermal aging experiments.

As discussed elsewhere [14], analysis of existing neutron, spallation proton and helium implantation data at intermediate temperatures (in the range of ≈250 to 400 °C) suggests that accumulation of a very high concentration of small He bubbles on grain boundaries reduces σ^*(IG). This results in a large amount of IG fracture, up to 100% in the most severe cases (see [14] and references therein). In combination with large $\Delta\sigma_y$, such He induced NHE could result in enormous and, indeed, unacceptable ΔT_i. Consider the following very simple conceptual model. Neglecting capillary, gas pressure and stress effects, for a given amount of He, the damaged area of a grain boundary scales with $1/r_b$, where r_b is the He bubble radius. Thus, although it is physically unlikely to happen, the most damaging condition for a given amount of He is a monolayer, or partial monolayer, of grain boundary coverage. Bubble distributions are finer at lower temperatures, while at high temperatures the He bubbles are coarser and would appear to cause less grain boundary damage. While less He would collect at grain boundaries at lower temperatures by purely thermal processes, radiation enhanced diffusion greatly increases solute transport rates. Thus, the critical amount of bulk He that causes IG fracture can be estimated based on collection of He from a region around a boundary over time, t, is $\approx 2\sqrt{D^* t}$, where D^* is the radiation enhanced He diffusion coefficient. Assuming a critical fraction of monolayer coverage f_{He} and a grain boundary thickness of ≈0.25 nm

$$C^*_{He}(\text{appm}) \approx 1.25 \times 10^{-4} f_{He}/\sqrt{(D^* t)}. \quad (10)$$

Since measurements are not available, estimates of the key parameter D^* require a detailed model, including the effects of recombination at high dose rates. At ≈300 °C a crude, but reasonable, estimate can be derived from the radiation enhanced diffusion rates of Cu [48], which is $D^* \approx 10^{-22}$ m^2/s for a dpa rate of $\approx 10^{-6}$/s. Assuming $f_{He} = 0.8$ and $t = 10^8$ s (100 dpa), $C^*_{He} \approx 1000$ appm, consistent with a He/dpa ratio of 10 appm/dpa. A critical bulk He concentration of 1000 appm is in reasonable agreement with our empirical estimates of the amount of He (>500 appm) that causes a significant contribution of NHE and IG fracture [14].

The possible NHE effects of high concentrations of H must also be considered. Hydrogen embrittlement would be expected to interact synergistically with both hardening and NHE, including grain boundary weakening due to fine-scale He bubbles. However, discussion of this important topic is beyond the scope of this paper.

2.5. An invariant master curve shape and dynamic microcrack propagation at length scales from 10^{-10} to 10^{-7} m (Fig. 7)

Within the framework of $\sigma^*(T)$–V^* type models, propagation of microcracks emanating from broken trigger particles is the fundamental atomic scale event controlling macroscopic cleavage. Propagation versus arrest is mediated by $K_\mu(T)$. While $K_\mu(T)$ is small (of order 2–3 MPa $\sqrt{m}$) it controls the corresponding continuum scale $K_{Jc}(T)$, which is much larger (> to ≫20 MPa $\sqrt{m}$). Thus, we have proposed that the invariant MC shape, $K_0(T - T_0)$, derives from an intrinsic $K_\mu(T)$

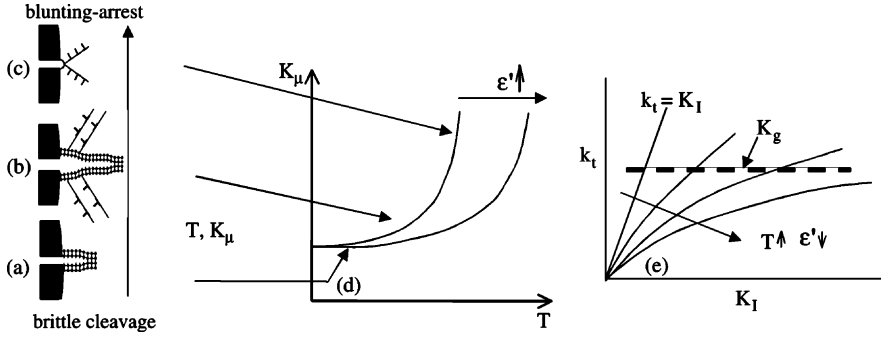

Fig. 7. (a) Illustration of brittle cleavage crack propagation from a trigger particle, (b) illustration of semi-brittle cleavage crack propagation from a trigger particle where crack blunting and shielding occurs by a small amount of dislocation emission and slip, (c) illustration of microcrack arrest by a large amount of dislocation emission and slip, (d) the $K_\mu(T)$ curve corresponding to the processes illustrated in (a)–(c), (e) the variation of k_t with K_I in a cleavage oriented crystal with increasing T and decreasing ε' showing a BDT when $k_t < K_g$ at high K_I.

of the ferrite lattice, or perhaps bcc lattices in general [5]. The K_μ is expected to depend on temperature and to undergo a brittle-to-ductile transition (BDT). The $\sigma^*(T)$–V^* model also assumes that $K_\mu(T)$ is not affected by the alloy microstructure, which may be more problematic. Thus, it is useful to seek guidance from basic models and experiments on cleavage and the BDT to better understand $K_\mu(T)$ and the factors that may control it. The BDT for cleavage in favorably oriented single crystal systems is a topic of a very large, and even more diverse, literature that is far beyond the scope of this paper to review. However, we will summarize the most salient research results to date.

Conceptually, most BDT $K_\mu(T)$-type models derive from the Rice–Thompson treatment of the 'cleavability' of a metal associated with suppression of dislocation emission from an atomically sharp crack tip [49]. Single crystal cleavage models seek to evaluate the remote loading conditions of increasing K_I that allow an initially *atomically sharp* crack to extend by cleavage. This is schematically illustrated in Fig. 7. If there is no dislocation activity at all, K_μ is approximately the fully brittle Griffith toughness, $K_I = K_g \approx 1$ MPa $\sqrt{m}$, given by Eq. (6) with $\gamma_p \approx 0$ (Fig. 7(a)). However, at all but the lowest temperatures and highest loading rates, or crack velocities, limited crack tip plasticity occurs by discrete dislocation emission and/or slip. Conceptually, the plastic work required for the emission and slip of even a small number of dislocations results in a significant $\gamma_p \gg \gamma$, and semi-brittle fracture. However, quantitative models must treat the sources and structures of the crack tip dislocations.

Dislocations may be emitted from the crack tip sites like ledges [50] and/or emanate from external sources [51,52]. The dislocations often, but not always, result in nanoscale blunting of the microcrack and reduce, or shield, the crack tip stress intensity factor, k_t, relative to the applied K_I, $k_t/K_I < 1$. Most models predict that an elastic dislocation free zone forms at the crack tip. Back stresses from the evolved dislocation structure reduce subsequent dislocation activity as K_I and k_t increase. High plastic strains and strain gradients also generate redundant dislocations that locally strengthen the material. Cleavage occurs *when*, *but only if*, $k_t = K_g$ at $K_I = K_\mu$. However, a larger level of dislocation activity can lead to conditions where k_t always remains less than K_g and $K_I/k_t \gg 1$, resulting in crack arrest (Fig. 7(c) and (e)).

The K_I/k_t and K_μ/K_g generally increase with higher dislocation nucleation rates and mobility, hence, in principle, also with increasing temperature and decreasing local strain rates (ε'). At very high ε' and very low temperatures, when lattice friction stress is very large, there is simply not time for dislocation generation and slip and $K_\mu \approx K_g$. In the opposite extreme, at high temperatures and low ε', there is little resistance to dislocation generation and/or extended slip; hence, the microcrack extensively blunts and arrests. Ignoring the effects of fine scale microstructure and very high velocity dislocation drag, the local dislocation mobility is primarily controlled by the thermally activated, lattice friction, or Peierl's stress, $\sigma_p(T, \varepsilon')$. Thus, as $\sigma_p(T, \varepsilon')$ decreases with increasing temperature or decreasing ε', $K_\mu(T)$ increases. The increase is initially gradual, but $K_\mu(T)$ ultimately undergoes a rapid upswing as it approaches the intrinsic bcc lattice BDT temperature (Fig. 7(d) and (e)). Since K_μ is actually for the arrest of a dynamic propagating microcrack, or at least a microcrack loaded at a very high stress intensity rate, the corresponding increase in $\sigma_p(T, \varepsilon')$ at high local ε' shifts $K_\mu(T)$ curve to higher temperature compared to static loading rates (Fig. 7(d)).

Various BDT models have been based on dislocation dynamics [33,51–59], continuum mechanics [60–62] and molecular dynamics [36,63] methods (and different combinations of them). Most, but not all [33], of the continuum and dislocation dynamics models are qualitatively consistent with a gradual initial increase in $K_\mu(T)$ with temperature above the $K_\mu \approx K_g$ shelf, as well as a strong effect of loading rate. The influence of the alloy microstructure is more complex. Pre-existing dislocations may act as easy sources for blunting and shielding, resulting in higher K_μ [51,52,64]; however, high densities of redundant dislocations also may restrict dislocation mobility, producing the opposite effect [65].

The BDT models also vary greatly in what they assume and the underlying physics they treat. Differences include static versus propagating cracks, straight versus ledged crack fronts, various sources and configurations of crack tip dislocations, various atomic and dislocation configurations leading to crack trapping, equilibrium versus dynamic dislocation positions, alternative constitutive-velocity laws and ways to couple to continuum plasticity, and a variety of stress field states (et cetera). Thus, the various BDT models predict such a wide range of results so that they can be picked, or adjusted, to be consistent with almost any experimental observation; and there is no clear and obvious basis to choose one over another. There are also a number of unresolved questions that have not even been addressed. These include the influence of: (a) finite blunting and three-dimensional geometry of the microcracks, realistic triaxial stress states and T-stresses; (b) accelerating crack velocities; (c) elastic modulus mismatches at the trigger particle-matrix interface; (d) local stress and strain concentrations and high dislocation densities at the trigger particles; and (e) the effects of fine scale dislocation obstacles. In summary, there are no rigorous models of $K_\mu(T)$.

Unfortunately, beyond the indirect estimates of K_μ and blunt notch assessments of $\sigma^*(T)$ described in Section 2.3 and limited single crystal $K_{Ic} = K_{Ix}$ data dis-

cussed below, there are relatively little reliable data to assess and verify the models. Another major shortcoming of many previous modeling studies is that they have been misdirected to predict macroscopic K_{Jc} rather than the microscopic K_{μ}; these are clearly very different entities. Certainly, three-dimensional single crystal cleavage models of high velocity, or at least rapidly loaded, cracks are needed and seem amenable to application of the evolving tools of modern dislocation and molecular dynamics. However, in the interim we return to available experimental observations.

A key puzzle is the apparent temperature and strain rate independence of σ^* found in a number of blunt notch tests [31,33–35,41–44]. Many previous studies covered only a limited temperature range, typically below 0 °C, where a constant σ^* is consistent with our assessment of $\sigma^*(T)$. However, in at least two cases, σ^* was approximately constant up to temperatures of ≈100 °C [31,42]. Interpretation of these results is complicated by the fact that the σ^*, or corresponding statistical model Weibull strength parameters, are different for blunt notches compared to the A^*–V^* cleavage criterion for cracks [39,40,66]. Cracks have higher, but more spatially localized, distributions of σ_n compared to the notches with lower but more broadly distributed stress fields. As a result, the estimated σ^* are typically higher for cracks than notches. However, it is not clear that the blunt notch σ^* is different than for cracks or is actually independent of temperature in self-consistent σ^*–V^* models [39]. Further, one recent study based on instrumented Charpy tests did suggest a mild temperature dependence of σ^* [67]. Thus, it will be important to revisit this issue using more reliable models and specially designed experiments to measure σ^* over a wide range of temperatures and crack tip σ_n fields.

The K_{μ} based on the σ^*–d_{tp} data (≈2.75 MPa $\sqrt{m}$) discussed in Section 2.3 are reasonably close to a number of measurements of very low temperature and/or high rate initiation toughness (K_{Ix}) for Fe, Mo and W single crystals oriented for cleavage initiated at very sharp pre-cracks [37,55,56,68–72]. Most single crystal K_{Ix} data show a strong effect of loading rate. However, the temperature dependence of $K_{Ix}(T)$ is generally even stronger than suggested by the $\sigma^*(T)$ described in Section 2.3. In part, this may be due to the large scale yielding resulting from the very low critical resolved shear stress of the single crystal metals, coupled with the small, atypical specimens often used in the K_{Ix} tests. The effect of temperature is somewhat suppressed in pre-cold worked W crystals, indicating a possible effect of a more complex microstructure as well as a higher strength [72].

There are very few data on the actual arrest toughness (K_{ax}) in single crystals. We have carried out preliminary crack arrest measurements for $\{1\,0\,0\}\langle 1\,0\,0\rangle$ cleavage in Fe at −196 and −150 °C [73]. Oriented single crystals are diffusion bonded into composite beam specimens and fatigue pre-cracked to a shallow a/W. The pre-cracked specimens are then loaded in a compression anvil fixture to initiate a propagating cleavage crack. The crack is initially 'driven' to higher velocities by a stress intensity factor, K_I, that increases with a/W. However, beyond a peak at $a/W \approx 0.2$, K_I decreases and the crack stops at an a/W determined by the arrest toughness K_{ax}. While K_{ax} may differ somewhat from the arrest of particle-nucleated microcracks, it involves similar atomic-dislocation-scale processes.

The average K_{ax} of the tests done to date are 4.4 ± 2.6 and 6.4 ± 2.6 MPa $\sqrt{m}$ at −196 and −150 °C, respectively. The corresponding median values were 3.6 and 4.9 MPa $\sqrt{m}$ and the minimum K_{ax} were 1.4 and 2.3 MPa $\sqrt{m}$. However, at −196 °C and, to a lesser extent, at −150 °C, the K_{ax} data appear to fall into low and high groupings. The mean K_{ax} are 3.1 ± 1.2 and 3.9 ± 1.2 MPa $\sqrt{m}$ at −196 and −150 °C, respectively, for the clusters of lower toughness data points. The single crystal surfaces show that cleavage crack propagation and arrest is very complex. A well-spaced series of very long slip traces is observed on the sides of specimens, indicating interim rapid arrest/re-initiation events. Slip steps, river patterns, ledges and facet-type features are observed on the cleavage fracture surfaces. This complexity may rationalize the rather high average and scattered K_{ax}. Attempts to measure the K_{ax} in Fe single crystals at higher temperatures have not yet been successful, but this work is continuing.

Qiao and Argon recently reported the results of an innovative approach to measuring K_{ax} in Fe–3%Si $\{1\,0\,0\}\langle 1\,0\,0\rangle$ cleavage oriented single crystals for cracks propagating up a temperature gradient [74]. The experiment involved a sequence of wedge loadings to initiate cleavage pop-in/arrest events up to a BDT temperature, where the crack simply blunted upon reloading. The average K_{ax} was 6.9 ± 0.75 MPa in the temperature range of ≈80 to 125 °C. Variations of K_{ax} with an effective loading rate were interpreted to show an activation energy of ≈0.1 eV [74]. This is similar to the activation energy for nucleation of double edge kinks in Fe alloys at high shear stress. Low activation energies (≈0.2 eV) have also been found for the loading rate dependence of K_{Ix} in W single crystals [72]. Notably, the activation energies for Fe and W are essentially identical when normalized by the corresponding ratio of their melting temperatures.

The thermal arrest K_{ax} at around 100 °C are generally higher than the K_{ax} we found for $\{1\,0\,0\}\langle 1\,0\,0\rangle$ cleavage in Fe at −196 and −150 °C. However, we found that fits to individual K_{ax}–T pairs of thermal arrest data show a significant temperature dependence with a $dK_{ax}/dT \approx 0.027 \pm 0.015$ MPa $\sqrt{m}$/°C. These results strongly support a dominant role of thermally activated dislocation slip in processes that govern $K_{ax}(T)$; indeed, it would be very difficult to rationalize these results on any other basis. A central role of dislocation slip is also

qualitatively consistent with the $\sigma^*(T)$ that we derived in the MC analysis of $K_{Jc}(T)$ in Section 2.3. Specifically we, and others, have noted that $\sigma^*(T)$ has a temperature dependence that is inverse to that for the lattice Peierl's stress [5,75].

The role of alloy microstructure remains unclear. In principle, fine scale pinning features in the 'vicinity' of the microcrack tip would also reduce K_μ by retarding slip. However, this is not consistent with the apparent insensitivity of σ^* to irradiation. As noted previously, the influence of dislocation structures is more complex, but very high densities would also generally be expected to reduce K_μ. However, the issue is not the effect of microstructure on the *magnitude* of K_μ but rather on its *temperature dependence*, which would still be controlled primarily by the activated lattice slip processes for a wide range of microstructures.

While it is an unresolved issue that will require additional modeling and experimental studies, we propose a simple new hypothesis for a minimal effect of pre-existing microstructure on the temperature dependence of $K_\mu(T)$. High stresses at trigger particles are accompanied by significant concentrations of plastic incompatibility strains, thereby producing high local dislocation densities. The dislocation densities would be increased further by the large local strain gradients. This would result in a much higher strength of the local ferrite matrix, and what might be viewed as an increase in the effective size of the trigger particle, perhaps, extending the cleavage regime to higher temperatures. Further, the dislocations that are formed before the particle cracks, would dominate the local microstructure, and may even destroy any fine scale pinning features. We hypothesize that, in effect, the initial propagation versus arrest of a particle-nucleated microcrack takes place in a local dislocation dominated microstructure that is relatively independent of the undeformed microstructure of the alloy.

In summary, the hypotheses of an approximately invariant $K_\mu(T)$ that mediates an approximately invariant MC $K_0(T-T_0)$ is broadly consistent with the analysis presented in this section. The temperature dependence of $K_\mu(T)$ is largely governed by thermally activated dislocation slip. Indeed, single crystal K_{Ix} and K_{ax} data generally show an even stronger temperature dependence than we found for $\sigma^*(T)$. Based on a variety of arguments, the temperature dependence of $K_\mu(T)$ is expected to be relatively insensitive to the pre-existing alloy microstructure. Specifically, it is likely that compatibility strain induced dislocations that form under loading prior to microcracking may dominate the local microstructure at the trigger particle.

Finally, we also note that the concepts outlined above also suggest a rapid increase in $K_\mu(T)$ near the actual lattice BDT temperature. This, in turn, may limit the maximum temperature of macroscopic cleavage. The temperature dependence of $K_\mu(T)$ in the upper BDT regime is not known. However, the thermal arrest data suggest a BDT temperature significantly greater than 125 °C, since K_μ is large (≈7 MPa $\sqrt{m}$) but is still increasing at a moderate rate (≈0.03 MPa $\sqrt{m}$/°C). The lattice BDT would place corresponding limits on the macroscopic cleavage regime even in the case of very large σ_y (and $\Delta\sigma_y$ due to irradiation). This may have important implications to the development of advanced, high strength cleavage resistant alloys.

2.6. Implications to embrittlement resistant alloys

The multiscale concepts outlined in the previous sections can guide the development of advanced high strength embrittlement resistant alloys, such as NFAs [76]. Assuming other microcrack formation mechanisms (like twin and dislocation pile-up nucleated cracks) do not intervene, or can be controlled by fine grain size, cleavage resistance can be enhanced by decreasing the size (thus increasing σ^*) and volume fraction (increased V^*) of the brittle trigger particles. This typically means eliminating carbides, as well as impurity inclusions and other brittle phases. The combined effects of the microstructure and alloy strength levels can be crudely evaluated in terms of a cleavage temperature (T_c) defined by the intersection of a elevated crack tip stress, σ_n with σ^*, as $\sigma_n = CF\sigma_y = \sigma^*$, where CF is a nominal constraint factor taken as ≈3. Note, this simplified treatment is more pertinent to blunt notches than cracks, but it still give a meaningful estimate of trends in T_c [31]. Representing $\sigma_y(T)$ as the sum of σ_y at 25 °C, σ_{yo}, and a temperature dependent term, $\approx \sigma_p(T)$, as

$$\sigma_p(T_c) + \sigma_{yo} = \sigma^*(T_c)/CF = K_\mu(T_c)[(\pi/2d_{pt})^{1/2}/CF]. \tag{11}$$

Fig. 8 illustrates the variation of T_c (indicated by the arrows) for $\sigma_{yo} = 500$, 1000, 1500 and 2000 MPa and $d_{tp} = 0.22$, 0.66 and 2 μm, CF = 3.0, $K_\mu(T) = 2 + 0.00333T$ (MPa $\sqrt{m}$), consistent with our $\sigma^*(T)$ analysis in Section 2.3, and a $\sigma_p(T)$ characteristic of ferritic and martensitic steels. The predicted T_c is above 300 °C at a very high $\sigma_{yo} = 2000$ MPa for $d_{tp} = 0.66$ μm, but decreases to ≈65 °C for $d_{tp} = 0.22$ μm. Thus within the framework of this very simple model, these results show that it may be possible to develop high toughness, high strength alloys (including a large irradiation induced $\Delta\sigma_y$) by controlling the trigger particle microstructures.

3. Recent progress on the MC–ΔT method

3.1. Models of size and geometry effects

The $\sigma^*(T)$–V^* model also provides a basis to treat extrinsic size and geometry effects on the measured K_{Jm}

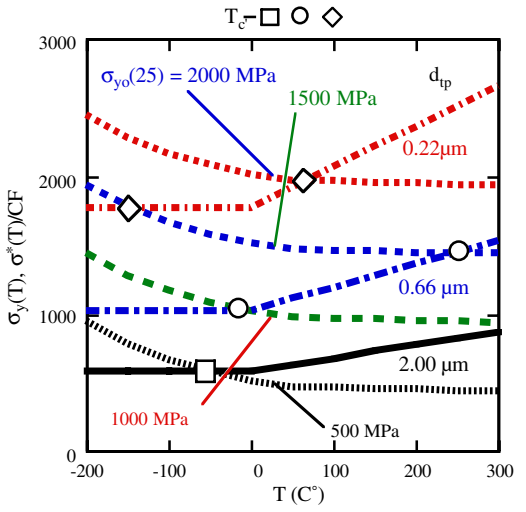

Fig. 8. Estimation of $T_{c'}$ temperatures for various combinations of σ_{yo} (25 °C) and $\sigma^*(T)/CF$ indicated by the circles, squares and diamonds. Higher σ_{yo} (25 °C) shift $T_{c'}$ up and smaller d_{tp} (hence, higher $\sigma^*(T)$) shift $T_{c'}$ down in temperature. For some combinations there is no intersection or a corresponding $T_{c'}$ below 300 °C. As one example, for σ_{yo} (25 °C) = 2000 MPa there is only one intersection for $d_{tp} = 0.22$ μm at $T_{c'} \approx 65$ °C.

[4,6,11,23–30]. As noted previously, when CL occurs in small specimens undergoing extensive plastic deformation, a larger K_J is needed to produce the same stressed volume $V(\sigma_n) = BA(\sigma_n)$ compared to the corresponding K_J for SSY conditions. Thus, it directly follows that $K_{Jm} > K_{Jc}$. Constraint is also lower in many common cracked-body geometries, such as shallow surface cracks, that lead to compressive T-stresses in the direction of crack advance [1,26–30]. Various methods have been used to model the effects of CL based on FE simulations of crack tip fields for a specified cracked-body size and geometry, $\sigma(\varepsilon)$ and local fracture properties. We have developed a *calibrated* constraint adjustment factor ($[K_{cl}/K_{ssy}]$) procedure, similar to the approach proposed by Dodds and co-workers [27]. [7] Here, $[K_{cl}/K_{ssy}]$ is the ratio of the larger K_J under conditions of CL (K_{cl}) that produces the same $V(\sigma_n)$ as a corresponding K_J for SSY (K_{ssy}). The $[K_{cl}/K_{ssy}]$ factor is used to adjust measured K_{Jm} to K_{Jc}, as $K_{Jm}/[K_{cl}/K_{ssy}]$. The constraint adjustment factor is a function of:

- The deformation level D, defined in Section 2 as $K_J^2/(E'\sigma_y b) \approx 2\delta/b$, where δ is the crack opening displacement and b is the uncracked ligament length.
- The material $\sigma(\varepsilon)$, or σ_y and a strain hardening law as, for example, represented by N, σ_y/E' (weakly) and σ^*.
- The cracked-body and loading geometry.

However, the constraint adjustment factor does not explicitly depend on A^*. Fig. 9(a) shows $[K_{cl}/K_{ssy}]$ as a function of D for the $\sigma(\varepsilon)$ and $\sigma^*/\sigma_y = 3$ of a typical A533B pressure vessel steel (Shoreham) at −91 °C for various B/W [23,25]. Fig. 9(b) shows $[K_{cl}/K_{ssy}]$ for various N as a function of σ^*/σ_y at $D = 0.02$ and plane strain conditions. It is also possible to translate K_{Jm} data from one CL condition to another; for example, from a small through crack bend specimen to a surface cracked thin walled structure in tension. The effects of CL can also be expressed in terms of changes in the shape of the $K_{Jc}(T)$ curves and/or ΔT_g temperature shifts at a specified K_{Jc}, [4,6]. Indeed, it is important to emphasize that toughness of any sort is only an intermediate quantity used to evaluate the P_c–Δ_c conditions for fracture of a cracked body. The procedures in Section 5 can be used to directly evaluate P_c–Δ_c for arbitrary geometry and loading levels.

Application of the constraint adjustment procedure requires experimental calibration of the σ^* as well as a $\sigma(\varepsilon)$ for a particular alloy. The σ^* can be estimated by fitting the $K_{Jc}(T - T_0)$ curve for a specified T_0 using Eqs. (6)–(8) [23–25]. A number of statistical elaborations of the deterministic σ^*–V^* models have been developed, including a recent calibrated Weibull stress model proposed by Dodds and co-workers [22]. The local loading parameter is the Weibull stress σ_w given by

$$\sigma_w = \left[\int \sigma_n^{m_\sigma} dV/V_0\right]^{1/m_\sigma}. \tag{12}$$

Here, the spatially varying crack tip σ_n, or principal, stress is power weighted by the Weibull stress modulus (m_σ) and volume integrated over a process zone normalized by an arbitrary reference volume V_0. Thus, σ_w and hence the probability of fracture, increases with increasing loading K_J. For a 3-parameter Weibull model, the corresponding probability (P_f) of cleavage fracture is

$$P_f = 1 - \exp\{-[(\sigma_w - \sigma_{min})/(\sigma_0 - \sigma_{min})]^{m_\sigma}\}. \tag{13}$$

Here σ_{min} is the minimum σ_w for cleavage fracture and $\sigma_0 = \sigma_w$ at $P_f = 0.63$. In principle, the m_σ, σ_0 and σ_{min} can be related to the underlying processes and microstructure. However, they are generally treated as empirical fit parameters for a particular material, loading rate and temperature. Calibration of the model requires data for both SSY and a variety of other constraint conditions [22,23].

[7] Note, these models are also consistent with the K–T and J–Q multi-parameter characterization methods proposed by a number of workers and described in Reference [1], as well as the statistical approach developed by Dodds and co-workers [22]. The most important difference between the various models is how they are calibrated to provide quantitative constraint loss adjustments for a particular alloy.

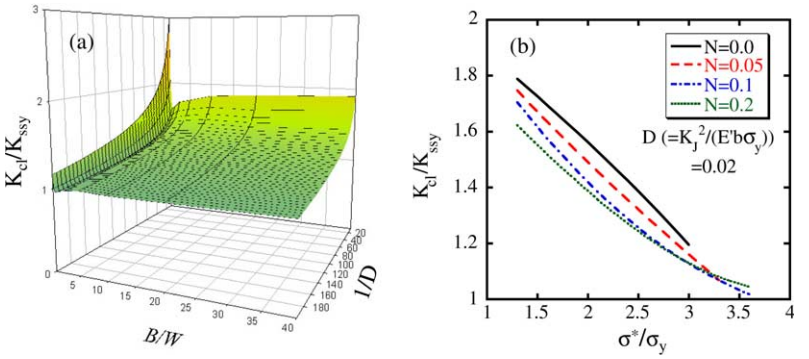

Fig. 9. (a) The $[K_{cl}/K_{ssy}]$ constraint adjustment factor as a function of D (actually $1/D$) and B/W from three-dimensional FE calculations for a 3PB specimen at $\sigma^*/\sigma_y = 3$ and $\sigma(\varepsilon)$ for the Shoreham RPV steel, (b) the $[K_{cl}/K_{ssy}]$ constraint adjustment factor as a function of σ^*/σ_y for various N at $D = 0.02$ for a plane strain 3PB specimen.

Statistical models also underpin the ASTM E1921 Master Curve Standard for measuring $K_0(T)$ in the cleavage transition [9,10]. Assuming a high level of constraint, for a specified specimen size (B), the probability of fracture (P_f) increases with the loading, K_J, as

$$P_f = 1 - \exp\{-[(K_J - K_{min})/(K_0 - K_{min})]^{m_k}\}. \quad (14)$$

Here m_k is the Weibull toughness modulus and K_{min} is a cleavage threshold toughness. In E1921 the m_k and K_{min} are fixed at 4 and 20 MPa $\sqrt{m}$ respectively. The $m_k = 4$ derives from the fact that for SSY the stressed volume, $V(\sigma_n)$, varies with K_J^4 for a specified B. Hence, it follows that for different B, $V^*(B_1) = V^*(B_2)$ when $K_{Jc}(B_2) = K_{Jc}(B_1)[B_1/B_2]^{1/4}$. However, $m_k \approx 4$ is consistent with experimentally observed Weibull distributions of K_{Jc} (or P_f) only if K_{min} is incorporated [1,10,23]. The fact that there is a threshold stress intensity for cleavage is physically intuitive. Further, the form of Eq. (14) for treating K_{min} derives from a mathematical representation of a conditional probability model assuming that cleavage fracture requires a sequence of two successful crack propagation events [1]. The value of $K_{min} = 20$ MPa $\sqrt{m}$ is the result of empirical fits to a large body of (mostly pressure vessel steel) data [10,77]. However, the $K_{min} = 20$ MPa $\sqrt{m}$ has no independent physical justification. Indeed, for $m_k \approx 4$, the best fit for K_{min} varies with temperature [78]. The best fit m_k and K_{min} combination is also likely to be material dependent.

However, assuming the nominal values of 4 and 20 MPa $\sqrt{m}$, statistical size effects of different specimen thickness (or crack front length) B follow from Eq. (14) with $P_f(B_1) = P_f(B_2)$ as,

$$K_{Jc}(B_2) = [K_{Jc}(B_1) - 20][B_1/B_2]^{1/m_k} + 20. \quad (15)$$

The reference K_{Jr} in E1921 is for $B = 25.4$ mm. We will refer to the adjustments provided by Eq. (14) as the $(B/B_r)^{1/4}$–K_{min} statistical size adjustment.

Constraint effects are not treated directly in E1921. However, the possibility of CL is recognized by a data censoring limit for deformation levels of $D = K_{Jm}^2/(E'b\sigma_y) > 0.033$ [9]. [8] This D applies to standard compact tension (CT) and 3PB specimens with $a/W \approx 0.5$ and B/W from 1 to 2. If there are enough valid data points, results from tests with K_{Jm} that exceed the $D = 0.033$ limit are replaced with a value of $[(E'b\sigma_y)/30]^{1/2}$, and used in a maximum likelihood estimate of the median toughness K_0 and T_0. In the past, the MC–ΔT method that we have proposed emphasized CL adjustments. However, more recently, statistical effects have also been incorporated as well. The MC–ΔT method is more flexible since it seeks to use the $K_0(T - T_0)$ shape most pertinent to the situation and allows use of optimized reference conditions.

3.2. Single variable experiments and model based analysis of size effects

Until recently, there has been no independent verification of many of the assumptions that underlie the ASTM E1921 Master Curve Standard. For example, most previous fracture tests used standard 3PB and CT specimens with $a/W \approx 0.5$ and B/W between 0.5 and 1. Since both the ligament (b) and thickness (B) varied in roughly the same proportion to the absolute specimen size, it was not possible to evaluate the relative contributions of the statistical, which we call B effects, versus CL, which we call D effects. That is, constraint loss effects could easily be mistaken for statistical effects. Indeed, earlier FE evaluations of $[K_{cl}/K_{ssy}]$ and data indicated that CL occurs at D significantly smaller than 0.033 [27,79,80]. Further, the deviations from SSY mimicked the statistical size scaling, but with K_{Jm} varying with $b^{-1/4}$, rather than $B^{-1/4}$ [79]. Notably, data

[8] The standard actually uses a limit of $M = 1/D = 30$.

sets subject to significant constraint loss bias T_0 towards the lower, non-conservative values, compared to more fully constrained conditions. Further, evaluation of the previously existing database did not fully support the $(B/B_r)^{1/4}$–K_{min} statistical size scaling [23,79]. Thus, we designed and carried out a single variable experiment to address the following questions [23]:

- What are the relative contributions of CL and statistical mediated size effects on K_{Jm}?
- Is the $(B/B_r)^{1/4}$–K_{min} statistical size scaling procedure consistent with toughness variations over a large range of B for conditions of high constraint?
- How do K_{Jm} and CL effects vary as a function of deformation?
- Is the $D = 0.033$ limit in E 1921–97 sufficient to avoid non-conservative bias in T_0 values compared to higher constraint conditions?
- Is there an effective and practical approach to adjusting for the combination of CL and statistical size effects and their interactions?

To answer these questions, a full matrix of $a/W \approx 0.5$ 3PB specimens with B from 8 to 254 mm and b from 3.2 to 25.4 mm were fabricated from the 3/4 thickness position in a A533B steel plate section of the Shoreham reactor vessel. The b–B test matrix covers an unprecedented range of specimen size and geometry. Eight specimens were tested under a common set of conditions at −91 °C for each b–B combination. The b–B database (184 data points in total) was analyzed with the $[K_{cl}/K_{ssy}]$ constraint and $(B/B_r)^{1/4}$–K_{min} statistical size adjustment procedures. Combined with this model-based analysis, the single variable b–B database allowed explicit de-coupling of statistical and constraint mediated size effects. Details can be found elsewhere [23–25,81,82].

Fig. 10(a) plots the K_{Jm} versus $\log B$ for the various b. The use of a log scale and the slight data point offsets for different b are for the purpose of clarity. The toughness generally decreases with increasing B, consistent with a statistical size effect. The mean $\langle K_{Jm}(B)\rangle$ for the largest $b = 25.4$ mm ($W = 50.8$) specimens was least squares fit

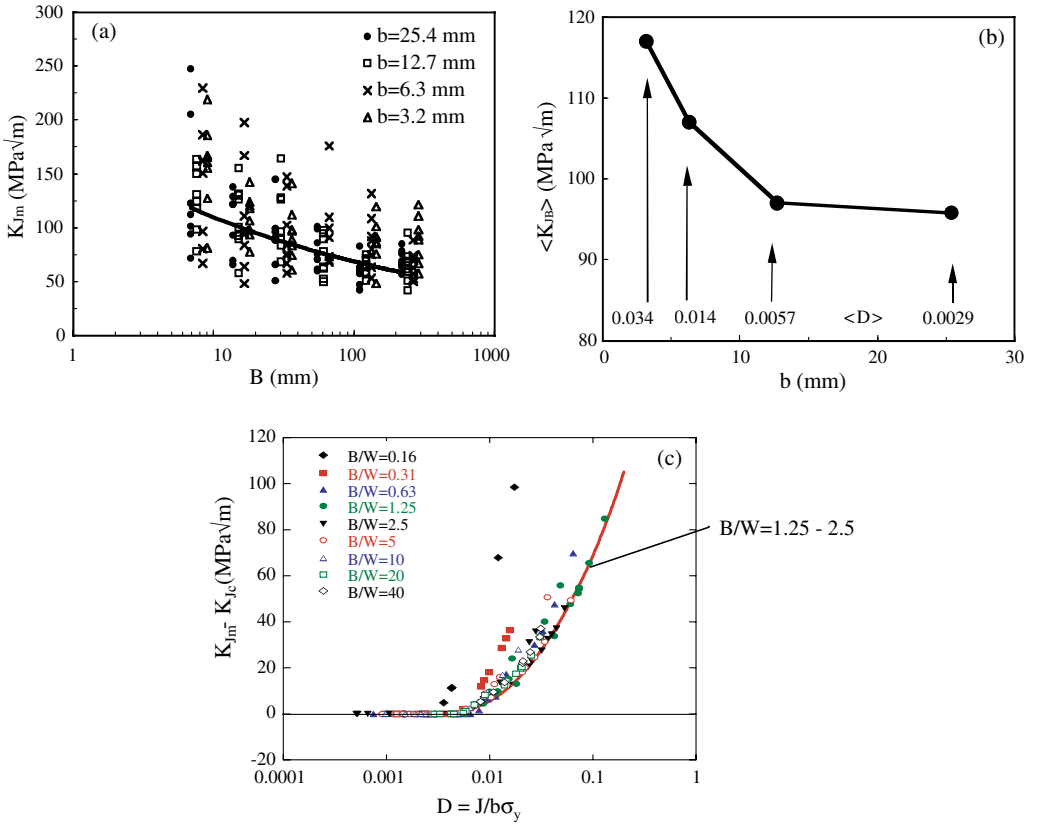

Fig. 10. (a) K_{Jm} versus B for the Shoreham steel b–B matrix and the best fit to the $W = 50$ mm data shown as the solid line, (b) the average $\langle K_{JB}\rangle$ following the $B^{-1/4}$–K^{min} statistical adjustment showing the effect of the loss of constraint for $b = 12.7$ and 6.3 mm, (c) the K_{Jm}–K_{Jc} for the Shoreham b–B test matrix, where K_{Jc} has been constraint adjusted by the $[K_{cl}/K_{ssy}]$ factor and the fit to the lower bound data for B/W at 1.25 and 2.5 shown as the solid line.

to the following inverted form of the $(B/B_r)^{1/4}$–K_{min} scaling equation

$$\langle K_{J_m}(B)\rangle = (\langle K_{J_m}(B_r)\rangle - 20)(B_r/B)^p + 20. \quad (16)$$

This gave $p = 0.26 \pm 0.09$, in almost exact agreement with the ASTM E1921 size scaling procedure. In general, the K_{J_m} are also larger for the specimens with smaller b, due to CL. The CL trend is better illustrated in Fig. 10(b), plotting $\langle K_{JB}\rangle = \langle[(K_{J_m} - 20)(B/B_r)^{1/4} + 20]\rangle$ as a function of b. Here $\langle K_{JB}\rangle$ is average K_{JB} found by adjusting K_{J_m} at various B to the reference thickness of $B_r = 25.4$ mm using Eq. (15). The average D for the various b are also shown. Significant CL is clearly observed at the two smallest b.

More generally, while Eq. (15) slightly over-adjusts the K_{J_m} data for the specimens with the largest B (the K_{J_r} are somewhat high), we found that the $(B/B_r)^{1/4}$–K_{min} statistical size adjustment is reasonably consistent with the overall b–B database. The $[K_{cl}/K_{ssy}]$ factor also slightly over-adjusts the K_{J_m} data (the K_{J_c} are slightly low on average) at the smallest b, particularly for two of the five B/b geometries. However, overall the constraint adjustment procedure was found to be very effective for a wide range of specimen sizes and deformation levels. After application of both the $[K_{cl}/K_{ssy}]$ constraint and the $(B/B_r)^{1/4}$–K_{min} statistical adjustments, the resulting K_{J_r} form a relatively homogeneous population, that is approximately independent of both specimen size (b) and geometry (B/W). The adjusted data give an ASTM E1921 $T_0 = -84$ °C [23–25].

These results show that for 3PB specimens, CL begins at deformation levels of $D < 0.01$ for $B/b > 1$ (encompassing the typical range of test specimen geometry of 1 to 2). This is much lower than the $D = 0.033$ censoring limit currently used in E1921. This is illustrated in Fig. 10(c) showing a plot of K_{J_m}–K_{J_c} versus D for the entire b–B database. We also applied the combined $[K_{cl}/K_{ssy}]$ and $(B/B_r)^{1/4}$–K_{min} adjustment procedure to an additional set of Shoreham K_{J_m} data we generated for the set of low constraint specimens. The adjusted K_{J_r} are also well represented by a MC with a $T_0 = -84$ °C, as found for the b–B database. Finally, the combined adjustment procedure was also applied to the large database on other plate sections of the Shoreham vessel reported by Tregoning and Joyce [83–85]. Again, the corresponding K_{J_r} are again well represented by a MC with a T_0 of −84 °C. The K_{J_m} and K_{J_r} for the entire 489 data points are shown in Fig. 11(a) and (b), respectively.

Quasi-cleavage is the dominant local fracture mode in 9Cr martensitic steels [26]. It has been postulated that a set of correlated sympathetic microfracture events along the crack front are necessary for macroscopic cleavage in general and quasi-cleavage in particular [19,20,26,86]. In principal, this could weaken the statistical size scaling compared to a single (or few) critical event mechanism. Thus, we have recently extended the b-B size effects study to Eurofer97. In this case, the b-B matrix is composed of 16 specimen configurations, with B ranging from 1.5 to 98 mm and the W range from 1.6 to 14 mm. Eight specimens will be tested at −142 °C for each of the 16 b-B combinations. The target median toughness is about 80 MPa $\sqrt{m}$, resulting in a nominal $D \approx 0.007$ for the $W = 14$ mm 'highest constraint' specimens. To date, only the $W = 14$ mm specimens have been tested. As shown in Fig. 12(a), the preliminary results clearly indicate that the Eurofer97 9Cr martensitic steel is also governed by $B^{-1/4}$-type statistical size scaling, except for the smallest $B = 1.5$ mm. In the latter case, with a very low $B/W \approx 0.11$, significant out-of-plane CL occurred. The constraint adjustments were minimal for the other B. Fig. 12(b) shows that the

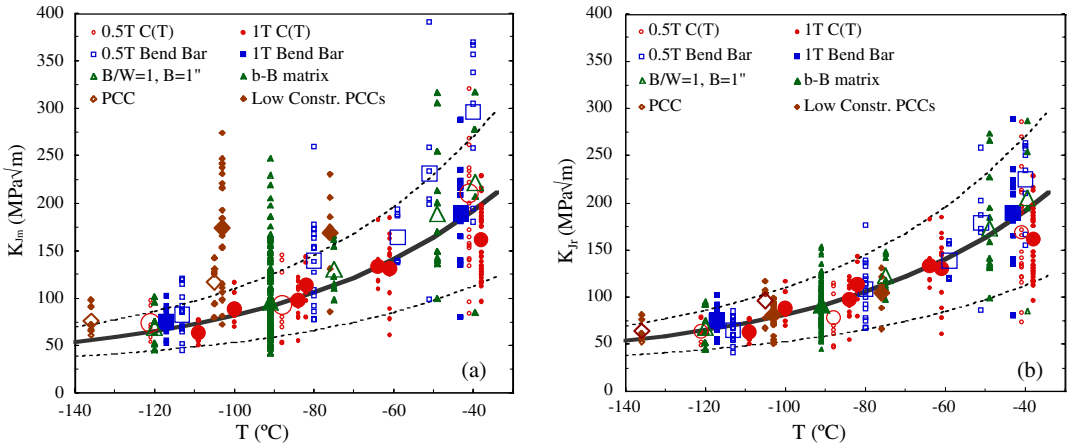

Fig. 11. (a) K_{J_m} for a 489 fracture tests on the Shoreham plate steels showing significant size effects and scatter around a MC with $T_0 \approx -84$ °C, (b) the corresponding size adjusted K_{J_r} data showing good agreement with a MC with $T_0 \approx -84$ °C.

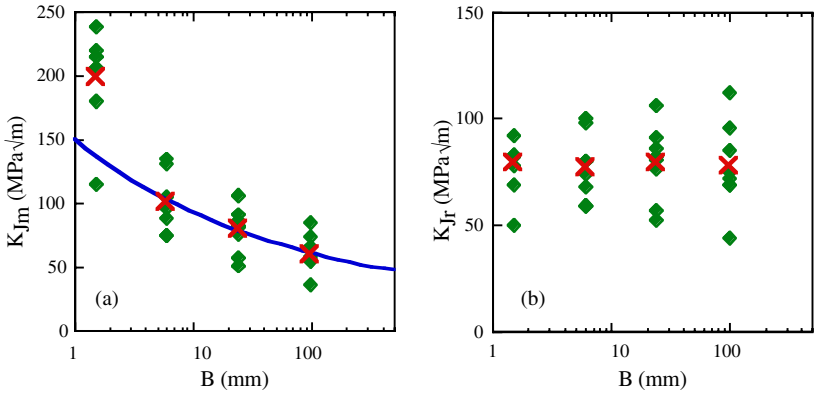

Fig. 12. (a) $K_{J\mathrm{m}}$ for a plate of the Eurofer97 9Cr martensitic steel as a function of B for tests at −142 °C on specimens with $W = 14$ mm, (b) the corresponding size-adjusted $K_{J\mathrm{r}}$ with a consistent average of $K_0 \approx 78 \pm 4$ MPa $\sqrt{\mathrm{m}}$.

combined $[K_{\mathrm{cl}}/K_{\mathrm{ssy}}]$ CL and $B^{-1/4}$–$K_{\min}$ statistical adjustments of $K_{J\mathrm{m}}$ results in a very consistent mean $K_{J\mathrm{r}} \approx 78 \pm 4$ MPa $\sqrt{\mathrm{m}}$ for all B. Tests on the remaining specimens in the b–B matrix, which will experience varying degrees of constraint loss, will be needed to fully calibrate the $[K_{\mathrm{cl}}/K_{\mathrm{ssy}}]$ model. Details will be presented elsewhere [87].

3.3. A master curve for a 9Cr martensitic steel

In Section 2.5, we proposed a basis for a constant $K_0(T - T_0)$ MC shape by assuming a moderate temperature dependence of intrinsic microcrack arrest toughness $K_{\mu}(T)$ of the ferrite matrix. Further, the size-adjusted $K_{J\mathrm{r}}(T)$ data in Fig. 12(b) are in good agreement with the MC shape over a wide range of temperature. However, a key question remains: does the E1921 $K_0(T - T_0)$, or other invariant shape, also apply to 9Cr martensitic steels, such as F82H and Eurofer97, both before and after irradiation? And if so, what are the limitations on the validity of this assumption? For example, it has been reported that in the case of a temper embrittled pressure vessel steel the $K_0(T - T_0)$ MC shape for cleavage does not work for IG fracture for K_0 more than ≈100 MPa $\sqrt{\mathrm{m}}$ [88]; and, there are indications that this may also be the case for conditions leading to IG fracture in F82H as well [88].

Fig. 13(a) summarizes the $K_{J\mathrm{B}}$ found by adjusting $K_{J\mathrm{m}}$ data on the International Energy Agency (IEA) heat of F82H that we have generated [8], [9] or found in the literature, to a reference $B_{\mathrm{r}} = 25.4$ mm [7,89–92]. The majority of this data was reported by Wallin for a wide range of specimen sizes [91]. We will again refer to the $[B/B_{\mathrm{r}}]^{1/4}$–$K_{\min}$ statistically adjusted data as $K_{J\mathrm{B}}$. Note the $K_{J\mathrm{B}}$ data are not constraint adjusted. The 1T CT data ($B = 25.4$ mm) reported by Wallin appear to follow MC shape up to very high levels of toughness. However, assuming SSY occurs up to about $D \approx 0.02$ for CT specimens, [10] the 1T CT $K_{J\mathrm{B}}$ data above ≈250 MPa $\sqrt{\mathrm{m}}$ would be expected to suffer some constraint loss. The sloping curves in Fig. 14(a) show the D limit of 0.01 for the 3PB specimens with various b. Clearly, most of the $K_{J\mathrm{B}}$ data from the smaller specimens suffers considerable CL.

Fig. 13(b) shows a preliminary constraint adjustment analysis of the F82H $K_{J\mathrm{m}}$ data. The adjustment was based on a lower bound fit to the $K_{J\mathrm{m}}$–$K_{J\mathrm{c}}$ results shown in Fig. 10(c). We provisionally assume that these Shoreham results are approximately applicable to F82H since the two steels have similar T_0. However, a fully calibrated $[K_{\mathrm{cl}}/K_{\mathrm{ssy}}]$ analysis is currently being carried out that will provide a much more accurate evaluation of the adjusted $K_{J\mathrm{r}}(T)$ data. In general, this improved procedure will further decrease the $K_{J\mathrm{r}}$ for the small specimens at $T < T_0$, thereby providing even better consistency between the F82H database and a single MC. Further details of this analysis will be given in a future publication [93]. However, given the potential effects of material inhomogeneity and other differences, these preliminary results clearly support the use of the E1921 MC for cleavage fracture in unirradiated 9Cr martensitic steels.

[9] Some of the UCSB data points have not been published. We also have generated a much larger amount of fracture data on an earlier heat of F82H that is similar to the results for the IEA heat [4,29,30] but this is not included in the compilation shown in Fig. 14.

[10] Deeply cracked CT specimens have a large positive (tensile) T-stress which *increases* constraint. Thus CL in this case occurs at higher levels of D, which we take here as 0.02.

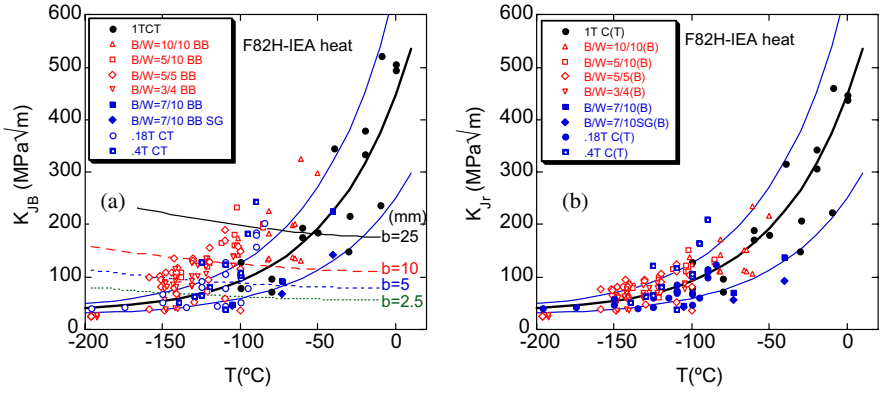

Fig. 13. (a) $B^{-1/4}$–K_{min} adjusted K_{JB} data (not constraint adjusted) or the IEA heat of F82H along with the constraint limits for various b assuming a maximum $D = 0.01$ along with the median and 5% and 95% MCs for $T_0 = -94$ °C, (b) the corresponding K_{Jr} based on the approximate constraint adjustment procedure described in the text.

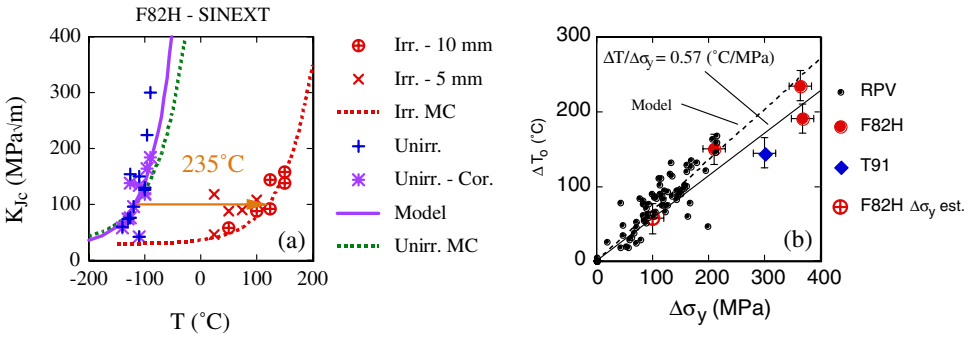

Fig. 14. (a) The effect of a ≈5 dpa 300 °C irradiation on the K_{Jm} and constraint adjusted (unirradiated only) K_{Jc} (asterisks) for the IEA heat of F82H showing a shift of ≈235 ± 25 °C, (b) ΔT_i versus $\Delta\sigma_y$ for ≈300 °C irradiations of the IEA heat of F82H and T91 along with a set of corresponding data for irradiated RPV steels. The solid and dashed lines show the best fits for these two cases, respectively.

3.4. The ΔT_0–$\Delta\sigma_y$ relation

There are very limited fracture toughness data on irradiated 9Cr martensitic steels. Fig. 14(a) shows K_{Jm} data as a function of temperature for the unirradiated IEA heat of F82H and following irradiation to ≈5 dpa at ≈300 °C [7,92]. The K_{Jm} were measured with CT specimens with $W = 22.5$ mm, $B = 10$ mm for the unirradiated condition and $B = 5$ and 10 mm for the irradiated condition. The $[K_{cl}/K_{ssy}]$ constraint adjusted K_{Jc} data are shown only for the unirradiated data. These adjustments are based on calibrating σ^* to a MC with the $K_{Jc}(T)$ model, shown by the solid line for a $T_0 = -115$ °C. This T_0 may be too low; hence, the $[K_{cl}/K_{ssy}]$ adjustments may underestimate the actual degree of CL. The irradiated data have not been constraint adjusted. However, even at the relatively low D up to ≈0.007, the thinner $B = 5$ mm specimens, with $B/W \approx 0.22$, fall systematically above the $B = 10$ mm CT data. A combination of both CL and statistical size effects result in the higher K_{Jm}. The $K_0(T - T_0)$ MC shape, shown as the dotted lines, provides a reasonable fit to both the constraint adjusted unirradiated and unadjusted irradiated $B = 10$ mm CT data. The irradiated data at $K_{Jm} > 150$ MPa $\sqrt{m}$ has a D of >0.014, and therefore may have experienced some CL. However, this has a relatively small effect on the estimated ΔT_i of ≈235 ± 20 °C.

The corresponding $\Delta\sigma_y$ for the 5 dpa 300 °C irradiation is ≈365 ± 25 MPa, thus the $\Delta T_i/\Delta\sigma_y$ is ≈0.64 ± 0.10 [7]. A set of ΔT_i and $\Delta\sigma_i$ data on an earlier heat of F82H and a T91 steel irradiated to ≈2–3 dpa at ≈300 °C resulted in estimates of $\Delta T_i/\Delta\sigma_y \approx 0.66 \pm 0.15$ and 0.52 ± 0.10, respectively [94]. Recent results reported by Sokolov et. al. on the IEA heat of F82 also give $\Delta T_i/\Delta\sigma_y \approx 0.52 \pm 0.10$ [89]. The ΔT_i versus $\Delta\sigma_y$ data are shown in Fig. 14(b), along with corresponding data for RPV steels complied by Sokolov [45]. The pressure vessel steel data are scattered, but have an average $\Delta T_i/\Delta\sigma_y \approx 0.69$ °C/MPa. This value is consistent with the prediction of the $K_{Jc}(T)$–$\Delta\sigma_y$ model with the fitted $\sigma^*(T)$ described in Section 2.3 shown as the dashed lines.

The fitted $\Delta T_i/\Delta\sigma_i \approx 0.57 \pm 0.13$ °C/MPa for the 9Cr martensitic steels, shown by the solid line, is somewhat lower, but generally within the observed scatter.

However, as discussed elsewhere [7], the lower $\Delta T_i/\Delta\sigma_y$ for the irradiated 9Cr martensitic steels, compared to the RPV steel data, may be primarily due to the effect of the high dose irradiations on the strain hardening (N) of these (and many other) alloys. Irradiations to a few dpa at temperatures below about 375 °C decrease the uniform engineering strain to <1% and reduce true strain hardening rates to very low values of $N < 0.05$. In contrast, lower dose 290 °C irradiations, characteristic of typical RPV conditions, have a relatively modest effect on strain hardening. The peak crack tip stresses actually scale with the flow stress $\sigma(\varepsilon)$ at $\varepsilon \approx 0.02$, rather than σ_y. Thus, it is more appropriate to correlate ΔT_i with $\Delta\sigma(0.02)$. For example, a $\Delta T_i/\Delta\sigma_y \approx 0.44 \pm 0.07$ °C/MPa was found for Eurofer97 irradiated to 2.7 dpa at a lower irradiation temperature of ≈60 °C [7,95]. The corresponding $\Delta T_i/\Delta\sigma$ (0.02) is ≈0.67 °C/MPa. The corresponding $\Delta T_i/\Delta\sigma$ (0.02) is ≈0.71 °C/MPa for the IEA heat of F82H irradiated to ≈5 dpa at ≈300 °C.

It is important to emphasize that the various measurements of ΔT_i and $\Delta\sigma_y$ are subject to significant uncertainties. Perhaps the major source of uncertainty is the irradiation temperature with typical variations of ≈ ±25 °C. At dose levels of about 3 dpa this alone translates into uncertainties in $\Delta\sigma_y$ of ≈ ±40 MPa and $\Delta T_i \approx \pm 25$ °C [14]. Given this, and several other potential sources of error and scatter, the $\Delta T_i/\Delta\sigma_y$ [or better $\Delta T_i/\Delta\sigma(\varepsilon)$] are remarkably consistent not only for the 9Cr martensitic steels themselves, but also with the larger pressure vessel steel database. The estimated $\Delta T_i/\Delta\sigma_y \approx 0.57 \pm 0.13$ °C/MPa is applicable to the irradiation temperature regime between ≈250 to 400 °C. A corollary is that since $\Delta\sigma_y$ up to 400 MPa, or more, may occur at higher doses at around 300 °C, very large $\Delta T_i \approx 260 \pm 40$ °C, or more, should be expected. *Thus, it is clear that 9Cr martensitic steels are not insensitive, let alone immune, to irradiation embrittlement.* At lower irradiation temperatures, the $\Delta T_i/\Delta\sigma(\varepsilon \approx 0.02)$ relation is more appropriate. And at irradiation temperatures higher than 400 °C (and higher doses), significant ΔT_i may arise from NHE mechanisms. Notably, these ΔT_i assessments *do not consider the potential synergistic embrittling effects of high concentrations of He and H*. We address further the issue of irradiation hardening and embrittlement elsewhere [14].

4. Structural implications of the multiscale fracture processes

It is clear from the discussion in the previous sections, as well as the data analysis presented in the companion report [14], that it will be necessary to manage irradiation hardening and embrittlement in the design and safe and reliable operation of FW&B structures. As we have repeatedly emphasized, the conditions leading to the fracture of a structure depend on many extrinsic details, as well as intrinsic local material properties. It is generally the objective of fracture testing to measure toughness in the most brittle coupon configuration possible. However, thin-walled, compliant FW&B structures, with small-shallow surface cracks loaded in tension are effectively much more fracture resistant than indicated by standard load controlled bend tests. Indeed, in some cases, FW&B structures may be immune to cleavage fracture. Further, since severe embrittlement is most often accompanied by large increases in σ_y, it is important to have a means of evaluating the structural trade-off between higher strength [11] and lower toughness. There may be conditions with $K_{Je} \gg K_{Jr}$ where the *structural benefits of increases in strength may outweigh the liabilities posed by irradiation embrittlement*.

In order to quantify these considerations, it is necessary to have proper structural metrics of performance. The most convenient and traditional measures are structural strength and ductility. For cracked structures, this can be expressed in terms of the ratios of the critical load and displacement at fracture (P_c and Δ_c) to those at general yielding (P_y and Δ_y). Clearly, high strength (P_c/P_y) and ductility (Δ_c/Δ_y) are desirable. The P_c and Δ_c can also be expressed in terms of the unirradiated condition (P_{co} and Δ_{co}) giving a direct measure of increased structural strength (P_c/P_{co}) and (generally) reduced ductility (Δ_c/Δ_{co}) due to in-service irradiation. In practice, however, it may be more feasible to specify a minimum ductility associated with a specific design (Δ_{cm}/Δ_y) and to recognize that P_c/P_{co} will be >1 as an extra safety margin. Various combinations of these (and other) structural performance indices can be used to construct integrity maps. Finally, this approach can quantitatively incorporate information from non-destructive flaw assessments and surveillance programs and be used in a probabilistic failure assessment methodology.

However, for purposes of further discussion, we will simply examine the effect of a small set of material and structural parameters on P_c/P_y and Δ_c/Δ_y. Further, while more complex and realistic cases can be analyzed, for convenience we will again use simple edge cracked 3PB geometry with various loading states and crack

[11] The issues of low uniform elongation and low toughness ductile tearing are also important and can also be dealt with in a systematic framework that is analogous to that outlined for fast cleavage fracture. However, these topics are beyond the scope of this paper.

configurations. The results are presented in terms of P/P_y versus Δ/Δ_y plots and the corresponding fracture loci of P_c/P_y and Δ_c/Δ_y as a function of the width (W) of the cracked beam. The plots also specify the conditions where cleavage is not possible within the framework of the model, and the corresponding conditions marking the nominal onset of ductile tearing. It is important to emphasize that these results are for the purpose of illustrating both the approach and significant trends; they do not provide a quantitative basis for general conclusions regarding the significance of embrittlement.

The plastic J_p, and Δ_p and the general yielding load P_y are based on the Electric Power Research Institute (EPRI) estimation scheme as summarized in Ref. [1] for a RO constitutive law defined by σ_y, N, $\varepsilon_y = \sigma_y/E$ and α as,

$$J_p \approx \alpha\varepsilon_y\sigma_y b h_1(a/W,N)(P/P_y)^{1/N+1}, \tag{17a}$$

$$\Delta_p \approx \alpha\varepsilon_y a h_3(a/W,N)(P/P_y)^{1/N}, \tag{17b}$$

$$P_y \approx 1.455Bb^2\sigma_y/S. \tag{17c}$$

Here, S is the loading span and h_1 and h_3 are tabulated geometric factors that are a function of a/W and N. The total J is given by the sum of the $J_p + J_e (= K_I^2/E')$ where K_I is the standard elastic stress intensity factor using a first order Irwin correction for an effective elastic–plastic crack length [1]. The total $\Delta = \Delta_p + \Delta_e$, where $\Delta_e = Z_{LL}P/(BE')$ and Z_{LL} is a standard elastic function of a/W.

First, we establish a brittle coupon type base case for comparison with the type of variations expected for actual FW&B structures. The base case parameters and their variants are listed in Table 1. In all cases, we assume a $K_{Jr} = 100$ MPa $\sqrt{m}$ for cleavage and $K_{Jc} = 150$ MPa $\sqrt{m}$ for ductile tearing, $\sigma_y = 730$ MPa and plane strain conditions. The most notable characteristics of the base case are a deep crack ($a/W = 0.5$) and long front ($B = 25.4$ mm) geometry for loading in 3PB with $1/N = 10$. The K_{Jc} are adjusted using Eq. (15) for the case with $B \neq 25.4$ mm. Fig. 15 shows P/P_y versus Δ/Δ_y for this base case (heavy solid line) along with the corresponding SSY $J/b\sigma_y$ (long dashed line). Constraint loss effects reduce the effective loading parameter for fracture (J_e) relative to the SSY J. The reduction of J_e relative to J depends on the fracture mode. We define a critical J_e at fracture as J_{ec}, where $J_{ec} = K_{Ie}^2/E'$ (or K_{Ie}^2/E'). For cleavage, we compute $J_{ec}/b\sigma_y$ (thinner solid line) based on the $[K_{cl}/K_{ssy}]$ adjustment procedure for plane strain, 3PB, $N = 0.1$ and $\sigma^*/\sigma_y = 3$. Note, there is a peak in the $J_{cc}/b\sigma_y$ curve, indicating that, according to the model, if cleavage has not occurred by this loading level it will not happen at larger P and Δ. This behavior is, to some extent, an artifact of the approximate constraint adjustment procedure. However, it does reflect a real effect of very rapid CL at high levels of deformation. For ductile tearing, we compute a corresponding $J_{ed}/b\sigma_y$ based on a CL adjustment procedure proposed by Anderson (short-long dashed line) [96]. The critical load (P_c) and displacement (Δ_c) where the $J_e = J_{Ic}$ value of the specified fracture mode then depends only on W.

Table 1
Parameters used to evaluate P–Δ curves and P_c/P_y–Δ_c/Δ_y fracture conditions

Parameters	Values
Specimen geometry	3PB in plain strain
Loading geometry	3PB
Specimen width: W	$W = 64, 32, 16, 8, 4$ (mm)
Specimen thickness: B	$B = 25.4$ (mm)
Crack length: a	$a/W = 0.5$
Span: S	$S/W = 4$
Constitutive properties	
E'	230 GPa
Yield stress	$\sigma_y = 725$ MPa
α	1
RO strain hardening exponent	$N = 0.1$
Critical stress ratio	$\sigma^*/\sigma_y = 3$
Toughness	
Cleavage initiation	$K_{Jc} = 100$ MPa $\sqrt{m}$
Ductile tearing initiation	$K_{Jc} = 150$ MPa $\sqrt{m}$

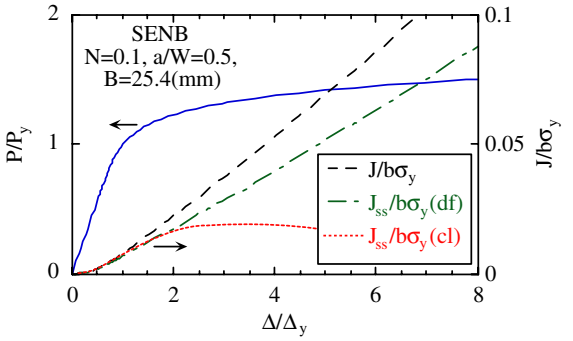

Fig. 15. P/P_y versus Δ/Δ_y (heavy solid line) and the effective J for SSY (dashed line) under conditions of CL for cleavage (thin solid line) and ductile fracture (long-short dashed lines).

For the corresponding P_c/P_y–Δ_c/Δ_y for $W = 64$, 32, 16, 8, and 6.3 (mm) for cleavage are plotted for the base case as open diamonds on the P/P_y–Δ/Δ_y curve in Fig. 16(a). The W^* is the smallest specimen where cleavage is possible according to the model. The conditions for the initiation of ductile tearing are shown as open squares. Thus, according to the model, an extra increment of P/P_y–Δ/Δ_y is needed for ductile crack extension for $W \leqslant 6.3$ mm. Plastic ductility, $\Delta_c/\Delta_y > 1$, occurs in

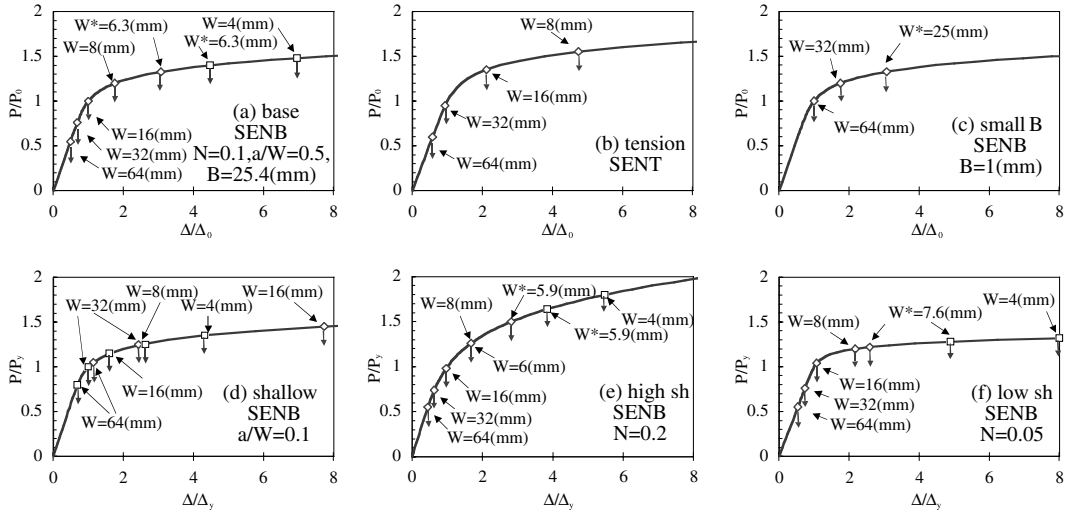

Fig. 16. P/P_y versus Δ/Δ_y showing the Δ_c/Δ_y for cleavage and ductile fracture as a function of W for various configurations and strain hardening (sh) rates. The W^* indicates the smallest W for cleavage predicted by the model. See text for further details.

specimens with $B < 16$ mm and becomes increasingly significant at smaller sizes even for this 'brittle' base case.

Fig. 16(b) shows that loading in tension versus bending approximately doubles Δ_c/Δ_y, and is accompanied by a substantial increase in the P_c/P_y as well as the W required for elastic fracture. The adjustment procedure we used in this case did not permit evaluation of an explicit W^*, but it would be larger than for the bending base case in Fig. 16(a). Fig. 16(c) shows the effect of a smaller, but perhaps more structurally realistic crack front length, of $B = 1$ mm. Statistical effects lead to a doubling of the K_{Jc} material toughness in this case and result in a much larger $W^* = 25$ mm. In effect, the model predicts that cleavage will not occur for small cracks in thin sections. Fig. 16(d) shows that a shallow crack with $a/W = 0.1$ (versus 0.5 for the base case) has a very large $\Delta_c/\Delta_y > 7$ for $W = 16$ mm. In this case, the constraint effects are such that ductile tearing occurs at a Δ_c/Δ_y that is lower than for cleavage. Fig. 16(e) and (f) show that increased strain hardening results in slight decreases in Δ_c/Δ_y and larger increases P_c/P_y.

These quantitative results should be interpreted to show only qualitative trends, since they are limited by the simplicity of the models we have used in the analysis. For example, there are cases where the model predicts that cleavage would not occur, when, in fact, experience shows that it does. However, while they are only to illustrate the approach to assessing general trends in structural P_c and Δ_c limits, these results clearly show that typical FW&B structures may be very resistant to brittle cleavage fracture. Key structural characteristics include small W (thin walls), small a/W (shallow cracks), small B (below future non-destructive examination detection or repair limits), primarily tensile and biaxial crack loading, low compliance and secondary stresses, as well as other beneficial effects such as warm pre-stressing.

5. Summary and conclusions

This paper provides a broad framework for the role of fracture mechanics and micromechanics, as well as the importance of irradiation embrittlement, in the design and operation of fusion FW&B structures. Our approach is based on a highly efficient MC–ΔT method for measuring and applying fracture toughness data $K_{Jc}(T)$ in the cleavage transition. The MC–ΔT method evaluates a reference temperature, T_0, that is used to index an invariant MC median toughness $K_0(T - T_0)$ shape. The T_0 is adjusted by temperature shifts, ΔT, that account for the effects of irradiation, loading rate and the size and geometry of the cracked body. We show that the $K_0(T - T_0)$ shape for pressure vessel steels is also applicable to cleavage fracture in 9Cr martensitic steels, and perhaps other bcc alloys as well. However, more generally, a small family of MC shapes may be needed to account for effects such as dynamic loading and IG fracture.

We demonstrate that the underpinning of the MC–ΔT method is a hierarchical multiscale sequence of processes starting on the atomic scale that ultimately control the cleavage fracture limits of large-scale fusion structures. This hierarchical approach to linking submodels for the various scales and processes is illustrated in the flowchart shown Fig. 17, along this the modeling and experimental tasks needed to develop a robust integrated fracture model. A detailed analysis of the existing hardening and embrittlement database and the

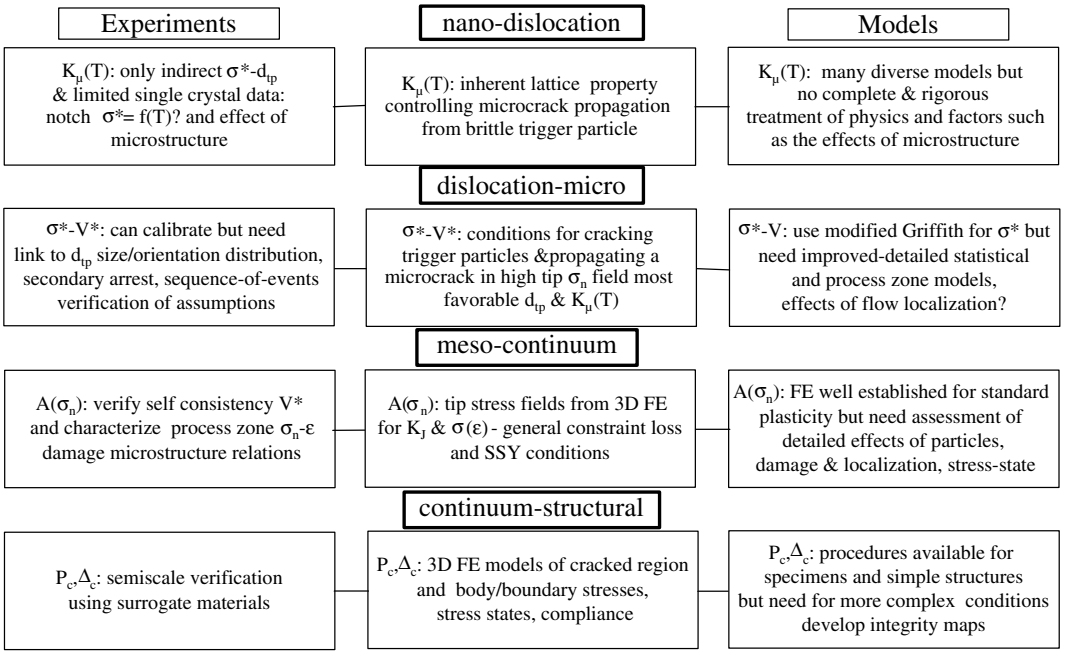

Fig. 17. Flowchart of the key 'properties' at various length scales that can be linked in a hierarchical model to relate atomic to structural scale processes that control cleavage fracture. Details are discussed in the text. Some of the modeling and experimental tasks needed to develop robust integrated models are shown. The approach can be extended to other failure modes.

corresponding implications to a future research agenda are presented in a companion report [14].

Atomic scale processes mediate the ferrite microarrest toughness, K_μ, that in turn determines the combination of the local crack tip normal stress, σ_n, and size, d_{tp}, of the largest trigger particle needed to nucleate a propagating microcrack. We propose that the intrinsic characteristics of the bcc ferrite lattice dictate an intrinsic temperature dependence of $K_\mu(T)$ that, in turn, lead to the invariance of the $K_0(T - T_0)$ MC. The local cleavage fracture criteria can be described in terms of a local critical stress, $\sigma^*(T)$, and stressed volume, V^*. The $\sigma^*(T)$ is governed by coarse-scale trigger particle microstructures and $K_\mu(T)$. The crack tip stress field conditions attaining σ^*–V^* can be related to the critical loads (P_c) and displacements (Δ_c), the cracked body size and geometry and the material constitutive law, $\sigma(\varepsilon)$. For restricted SSY conditions, a unique K_{Jc} can characterize cleavage fracture toughness.

The $K_{Jc}(T)$ curve can be modeled in terms of the intrinsic elastic modulus, E', and microstructurally dependent σ^*, V^* and $\sigma(\varepsilon)$. The effects of irradiation are generally due to the corresponding effects on $\sigma(\varepsilon)$. Increases in the yield stress, $\Delta\sigma_y$, due to irradiation (or higher strain rates) shift the $K_{Jc}(T)$ curve by ΔT_i to a higher T_{0a}. However, the effects on ΔT_i are reduced somewhat by the decreased rate of strain hardening, ΔN, due to irradiation. The importance of this effect increases with decreasing irradiation temperature. Typical values of $\Delta T_i/\Delta\sigma_y$ for intermediate temperature (≈300 °C) and dose (1–10 dpa) fission reactor irradiations of 9Cr martensitic steels are ≈0.6 ± 0.1 °C/MPa and ΔT_i of 260 °C or more can be expected from irradiation hardening alone.

However, there are also a number of possible sources of NHE. Significant NHE is signaled by large or even negative (for softening conditions) values of $\Delta T_i/\Delta\sigma_y$ and, often, increasing amounts of IG fracture. Hardening and NHE interact synergistically and can lead to very large and, perhaps, unacceptable ΔT_i. A significant amount of He on grain boundaries in the form of fine bubbles can cause NHE. Further, very high matrix He may contribute an increment to $\Delta\sigma_y$. The effect of He depends on a number of details, but in the companion report we estimate the critical quantity for a significant embrittlement contribution to be between 500 and 700 appm for irradiations around 300 °C. High levels of H may also increase ΔT_i further.

Multiscale processes also play a role in the extrinsic size and cracked-body geometry dependence of cleavage fracture toughness, which, generally, cannot be characterized by a unique intrinsic K_{Jc}. The measured K_{Jm} from coupon tests and effective K_{Je} pertinent to a structure are typically greater, and may be much greater, than K_{Jc}. Size and geometry effects arise from both statistics related to the magnitude of the highly stressed volume

near the crack tip and CL associated with cleavage after large amounts of deformation in small specimens or for typical shallow tensile loaded surface cracks. We show that statistical effects are similar in 9Cr martensitic and RPV pressure vessel steels leading to a scaling of toughness with the effective crack front length, B, as $\approx B^{-1/4}$. The actual statistical scaling applies to the K_{Jc} in excess of a minimum threshold toughness, $K_{min} \approx 20$ MPa $\sqrt{m}$. We also show that micromechanical models can be used to adjust K_{Jm} measured under conditions of CL in small specimen testing to K_{Jc} as well as to K_{Je}, for conditions of constraint pertinent to a structure.

Finally, we show by a simple example the profound implications of size scaling to structures based on a metric of strength and ductility. These are specified as the ratios of the critical load and displacement at fracture to the yield load and displacement, or P_c/P_y and Δ_c/Δ_y, respectively. Even in cases where the material is very brittle based on standard coupon testing, or in heavy section applications, the extrinsic factors typical of FW&B structures (small crack depth and front length, wall thickness and tensile loading) lead to $P_c/P_y > 1$ and $\Delta_c/\Delta_y \gg 1$. Hence, up to some point, embrittled 9Cr martensitic may provide acceptable performance in these applications. Indeed, in some cases the beneficial effects of irradiation on increasing P_c may more than offset the liabilities of the decreases in Δ_c.

Acknowledgements

The authors wish to thank a number of people that have contributed to this work over the years, including R.J. Kurtz, G.E. Lucas, P. Spatig, D. Gragg, K. Edsinger, E. Donahue, M. He, H. Kishimoto and J.W. Sheckherd, as well as many others in the worldwide fusion and fusion materials research communities too numerous to mention. The US Department of Energy Office of Fusion Science (DE-FG03-94ER-5475) provided the primarily support for the UCSB research described in this paper, with additional contributions from the US Nuclear Regulatory Commission (NRC-04-01-064). Thus we also thank our program monitors Sam Berk (DOE) and Tanny Santos (NRC) for their encouragement and support.

References

[1] T.L. Anderson, Fracture Mechanics Fundamentals and Applications, 2nd Ed., CRC, 1995.
[2] B. van der Schaff et al., J. Nucl. Mater. 283–287 (2000) 52.
[3] R. Klueh et al., J. Nucl. Mater. 307–311 (2002) 455.
[4] G.R. Odette, K. Edsinger, G.E. Lucas, E. Donahue, Small Specimen Test Techniques, ASTM STP 1329, 1998, p. 298.
[5] G.R. Odette, M.Y. He, J. Nucl. Mater. 283–287 (2000) 120.
[6] G.R. Odette, M.Y. He, J. Nucl. Mater. 307–311 (2002) 1624.
[7] G.R. Odette, H.J. Rathbun, J.W. Rensman, F.P. van den Broek, J. Nucl. Mater. 307–311 (2002) 1624.
[8] P. Spatig, G.R. Odette, E. Donahue, G.E. Lucas, J. Nucl. Mater. 283–287 (2000) 120.
[9] ASTM E 1921-02, Standard Test Method for Determination of Reference Temperature, T_0, for Ferritic Steels in the Transition Range, ASTM, 2002.
[10] J.G. Merkle, K. Wallin, D.E. McCabe, Technical Basis for an ASTM Standard on Determining the Reference Temperature, T_0, for Ferritic Steels in the Transition Range, NUREG/CR-5504, 1998.
[11] E.G. Donahue, G.R. Odette, G.E. Lucas, J. Nucl. Mater. 283–287 (2000) 518.
[12] G.R. Odette, B.D. Wirth, D.J. Bacon, N.M. Ghoniem, MRS Bull. (2001) 176.
[13] S. Jumel et al., J. Test Eval. 30-1 (2002) 37.
[14] T. Yamamoto, H. Kishimoto, G.R. Odette, Fusion Materials Semiannual Report 7/1 to 12/31/2003 DOE/ER-313/34 to be published (a shorter version of this will also be submitted for publication in the proceedings of ICFRM 11).
[15] ABAQUS/Standard User's Manual, Version 6.3, Hibbitt, Karlsson & Sorensen, Inc., 2002.
[16] F.M. Beremin, Met. Trans. 14A (1983) 2277.
[17] K. Wallin, Eng. Fract. Mech. 22 (1985) 149.
[18] K. Wallin, Eng. Fract. Mech. 19 (1985) 1085.
[19] T. Lin, A.G. Evans, R.O. Ritchie, J. Mech. Phys. Solids 34-5 (1986) 477.
[20] A.G. Evans, Met. Trans. 14A (1983) 1349.
[21] G.R. Odette, B.L. Chao, G.E. Lucas, J. Nucl. Mater. 191–194 (1992) 827.
[22] X. Gao, C. Ruggieri, R.H. Dodds Jr., Int. J. Fract. 92 (1998) 175.
[23] H.J. Rathbun, G.R. Odette, M.Y. He, G.E. Lucas, T. Yamamoto, NUREG/CR 6790, 2003, in press.
[24] H.J. Rathbun, G.R. Odette and M.Y. He, in: Proceedings of the International Congress on Fracture, vol. 10, 2001.
[25] H.J. Rathbun, G.R. Odette, M.Y. He, T. Yamamoto, G.E. Lucas, in: Application of Fracture Mechanics in Failure Assessment, ASME PVP 462 (2003) 31.
[26] G.R. Odette, J. Nucl. Mater. 212–215 (1994) 45.
[27] M. Nevalainen, R.H. Dodds, Int. J. Fract. 74 (1995) 131.
[28] M. Enmark, K. Edsinger, G.E. Lucas, G.R. Odette, J. Nucl. Mater. 233–237 (1996) 347.
[29] G.E. Lucas, G.R. Odette, K. Edsinger, B. Wirth, J.W. Sheckherd, in: Effects of Irradiation on Materials – 17th International Symposium, ASTM STP 1270, 1996, p. 790.
[30] K. Edsinger, G.R. Odette, G.E. Lucas, J.W. Sheckherd, J. Nucl. Mater. 233–237 (1996) 342.
[31] G.R. Odette, P.M. Lombrozo, R.A. Wullaert, in: Effects of Irradiation on Materials – 11th International Symposium, ATM STP 870, 1985, p. 841.
[32] R.O. Ritchie, J.F. Knott, J.R. Rice, J. Mech. Phys. Solids 21 (1973) 395.
[33] S.G. Roberts, S.J. Noronha, A.J. Wilkinson, P.B. Hirsh, Acta Mater. 50 (2002) 1244.
[34] G.T. Hahn, Met. Trans. 15A (1984) 947.
[35] P. Bowen, S.G. Druce, J.F. Knott, Acta Metall. 34 (1986) 112.

[36] S. Kohlhoff, P. Gumbsch, H.F. Fishmeister, Philos. Mag. A 64 (4) (1991) 851.
[37] W.W. Gerberich, H. Huang, W. Zielinski, P.G. Marsh, Met. Trans. 24A (1993) 53.
[38] W-J. Yang, B-S. Lee, M-Y. Huh, J-H. Hong, J. Nucl. Mater. 317 (2–3) (2003) 234.
[39] T. Yamamoto, G.R. Odette, G.E. Lucas, H. Matsui, J. Nucl. Mater. 283–287 (2000) 992.
[40] T. Saario, Wallin, K. Torronen, J. Eng. Mater. Technol. 108 (1984) 173.
[41] D.A. Curry, J.F. Knott, Met. Sci. 12 (1978) 511.
[42] J.R. Griffiths, D.R.J. Owen, J. Mech. Phys. Solids 19 (1971) 419.
[43] D.A. Curry, Met. Sci. 16 (1982) 435.
[44] R. Sandstrom, Y. Bergstrom, Met. Sci. 18 (1984) 177.
[45] M.A. Sokolov, R.K. Nanstad, Effects of Irradiation on Materials – 18th International Symposium, ASTM STP 1325, 1999, p. 167.
[46] L. Schafer, M. Shirra, J. Nucl. Mater. 271–272 (1999) 455.
[47] K. Shiba, in: Proceedings of the IEA Workshop/Working Group Meeting on Ferritic/Martensitic Steels, ORNL/M-6627, 1998.
[48] G.R. Odette, T. Yamamoto, D. Klingensmith, Philos. Mag. A, submitted for publication.
[49] J.R. Rice, R. Thompson, Philos. Mag. 15 (1974) 567.
[50] X. Zu, A.S. Argon, Philos. Mag. A 72 (2) (1995) 415.
[51] S. Mesarovic, J. Mech. Phys. Solids 45 (2) (1997) 211.
[52] S.G. Roberts, A.S. Booth, P.B. Hirsh, Mat. Sci. Eng. A 176 (1994) 91.
[53] M.L. Jokl, V. Vitek, C.J. McMahon Jr., Acta Metall. 28 (1980) 1497.
[54] R-H. Zhao, S-H. Dai, J.C.M. Li, Int. J. Fract. 29 (1985) 3.
[55] H. Huang, W.W. Gerberich, Acta Metall. Mater. 42 (3) (1994) 639.
[56] P.G. Marsh, Acta Metall. Mater. 42 (3) (1994) 613.
[57] P. Hahner, H. Stamm, Acta Metall. Mater. 43 (7) (1995) 2797.
[58] M. Große Gehling, V. Vehoff, Mat. Sci. Eng. A 278 (2000) 213.
[59] P. Gumbsch, Mat. Sci. Eng. A 319 (2001) 1.
[60] P.A. Matega, L.B. Freund, J.W. Hitchninson, J. Phys. Chem. Solids 48 (11) (1987) 985.
[61] V.R. Nitzsche, K.J. Hsia, Mat. Sci. Eng. A 176 (1994) 155.
[62] G.E. Beltz, J.R. Rice, C.F. Shih, L. Xai, Acta Mater. 44 (10) (1996) 3943.
[63] M. Mullins, M.A. Dokainish, Philos. Mag. A 46 (1982).
[64] M.F. Ashby, J.D. Embury, Scr. Metall. 19 (1985) 557.
[65] D.M. Lipkin, D.R. Clarke, G.E. Beltz, Acta Mater. 44 (10) (1996) 4051.
[66] T. Lin, A.G. Evans, R.O. Ritchie, Acta Metall. 34 (11) (1986) 2205.
[67] A. Fabry, Small Specimen Test Techniques, ASTM STP 1329, 1998, p. 274.
[68] A.S. Argon, J. Eng. Mater. Technol. 123 (2001) 1.
[69] J.J. Gilman, J. Appl. Phys. 31 (1960) 2208.
[70] D. Hull, P. Beardmore, A.P. Valintine, Philos. Mag. 12 (1965) 1021.
[71] P. Marsh, H. Huang, W.W. Gerberich, Acta Metall. Mater. 40 (1992) 2883.
[72] P. Gumbsh, J. Riedle, A. Hartmaier, H. Fishmeister, Science 282 (13) (1998) 1293.
[73] M. Hribernik, G.R. Odette, unpublished research.
[74] Y. Qiao, A.S. Argon, Mech. Mat. 35 (2003) 903.
[75] K. Wallin, T. Saario, K. Torronen, Met. Sci. 18 (1984) 13.
[76] M.J. Alinger, G.R. Odette, G.E. Lucas, J. Nucl. Mater. 307–311 (2002) 484.
[77] K. Wallin, Eng. Frac. Mech. 69 (4) (2002) 451, see also other papers in special issue on the E1921 master curve method.
[78] R.H. Dodds, Jr., personal communication.
[79] H.J. Rathbun, G.R. Odette, M.Y. He, G.E. Lucas, J.W. Sheckherd, Fracture Fatigue and Weld Residual Stress, ASME PVP, vol. 393, 1999, p. 17.
[80] H.J. Rathbun, G.R. Odette, M.Y. He, Applications of Fracture Mechanics in Failure Assessment, ASME PVP, vol. 412, 2000, p. 113.
[81] H.J. Rathbun, G.R. Odette, M.Y. He, T. Yamamoto, J. Eng. Fract. Mech., in preparation.
[82] H.J. Rathbun, G.R. Odette, M.Y. He, T. Yamamoto, Eng. Fract. Mech., in preparation.
[83] J.A. Joyce, R.L. Tregoning, Eng. Fract. Mech. 68 (7) (2001) 861.
[84] R.L. Tregoning, J.A. Joyce, Fatig. Fract. (2001).
[85] R.L. Tregoning, J.A. Joyce, Applications of Fracture Mechanics in Failure Assessment, ASME PVP 412, 2000.
[86] W.W. Gerberich, S.-H. Chen, C.-S. Lee, T. Livne, Met. Trans. 18A (1987) 1861.
[87] J.-W. Rensman, R. Yasuda, G.R. Odette, F.J. Blom, T. Yamamoto, D. Gragg, J. Nucl. Mater., in preparation.
[88] M. Sokolov, personal communication.
[89] M. Sokolov, R. Klueh, G.R. Odette, K. Shiba, H. Tanaigawa, Effects of Irradiation on Materials – 21st International Symposium, ASTM STP 1447, in press.
[90] P. Spatig, E. Donahue, G.R. Odette, G.E. Lucas, M. Victoria, Mater. Res. Soc. (2001) Z7.8.
[91] K. Wallin, A. Laukkanen, S. Tahtinen, Small Specimen Test Techniques 4, ASTM STP 1418, 2002, p. 33.
[92] J.-W. Rensman et al., J. Nucl. Mater. 307–311 (2002) 245.
[93] G.R. Odette, M. He, G.E. Lucas, J. Nucl. Mater., in preparation.
[94] E. van Osh, M. Horsten, G.E. Lucas, G.R. Odette, Effects of Radiation on Materials – 19th International Symposium, ASTM STP 1366, 2000, p. 613.
[95] J.-W. Rensman et al., J. Nucl. Mater. 307–311 (2002) 250.
[96] T.L. Anderson, N.M.R. Vanaparthy, R.H. Dodds Jr., Constraint Effects in Fracture, ASTM STP 1171, 1993, p. 473.